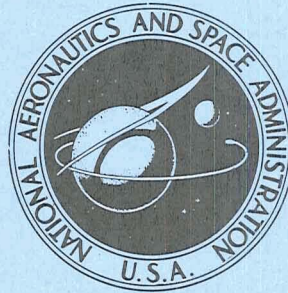


N71-32165

NASA TECHNICAL
MEMORANDUM



NASA TM X-2342

NASA TM X-2342

CASE FILE
COPY

CASE FILE
COPY

EFFECT OF VELOCITY PROFILE DISTORTION
IN LONG dc ELECTROMAGNETIC FLOWMETERS

by Shee-Ming Chen

*Lewis Research Center
Cleveland, Ohio 44135*

1. Report No. NASA TM X-2342	2. Government Accession No.	3. Recipient's Catalog No.	
4. Title and Subtitle EFFECT OF VELOCITY PROFILE DISTORTION IN LONG dc ELECTROMAGNETIC FLOWMETERS		5. Report Date August 1971	6. Performing Organization Code
		8. Performing Organization Report No. E-6259	10. Work Unit No. 128-31
7. Author(s) Shee-Ming Chen	9. Performing Organization Name and Address Lewis Research Center National Aeronautics and Space Administration Cleveland, Ohio 44135		11. Contract or Grant No.
12. Sponsoring Agency Name and Address National Aeronautics and Space Administration Washington, D.C. 20546			13. Type of Report and Period Covered Technical Memorandum
		14. Sponsoring Agency Code	
15. Supplementary Notes			
16. Abstract To make precision liquid-metal flow rate measurements using a dc electromagnetic flowmeter it is necessary to consider such effects as the distortion of the velocity profile by the magnetic field and the entry and exit processes at the edges of the magnetic field. In this study, the distorted velocity profile and corresponding electric potential distribution are determined using a two-dimensional model in simulation of a long electromagnetic flowmeter. The method of finite differences is used in solving the magnetohydrodynamic equations for a circular pipe with either a non-conducting or conducting wall. Calibration curves, as well as numerical solutions for the velocity and potential distributions over the pipe cross section, are obtained for various combinations of fluid and wall conductivity, thickness of the pipe wall, and Hartmann number.			
17. Key Words (Suggested by Author(s)) Flowmeter, Flow measurement, Liquid metals, Magnetohydrodynamics, Velocity profiles, Flow distribution, Velocity distribution, Flow distortion		18. Distribution Statement Unclassified - unlimited	
19. Security Classif. (of this report) Unclassified	20. Security Classif. (of this page) Unclassified	21. No. of Pages 40	22. Price* \$3.00

* For sale by the National Technical Information Service, Springfield, Virginia 22151

CONTENTS

	Page
SUMMARY	1
INTRODUCTION	1
THE MODEL	4
BASIC EQUATIONS AND BOUNDARY CONDITIONS	4
PREVIOUS RESULTS	8
NUMERICAL METHOD	10
RESULTS	13
CONCLUDING REMARKS	17
APPENDIX - SYMBOLS	18
REFERENCES	20

EFFECT OF VELOCITY PROFILE DISTORTION IN LONG dc ELECTROMAGNETIC FLOWMETERS

by Shee-Ming Chen*

Lewis Research Center

SUMMARY

To make precision liquid-metal flow rate measurements using a dc electromagnetic flowmeter it is necessary to consider such effects as the distortion of the velocity profile by the magnetic field and the entry and exit processes at the edges of the magnetic field. In this study, the distorted velocity profile and corresponding electric potential distribution are determined using a two-dimensional model in simulation of a long electromagnetic flowmeter. The method of finite differences is used in solving the magnetohydrodynamic equations for a circular pipe with either a nonconducting or conducting wall. Calibration curves, as well as numerical solutions for the velocity and potential distributions over the pipe cross section, are obtained for various combinations of fluid and wall conductivity, thickness of the pipe wall, and Hartmann number.

INTRODUCTION

Electromagnetic flowmeters use the principle that material moving in a magnetic field experiences an electric field in a direction perpendicular to both the magnetic field and the motion. The voltage resulting from the electric field gives a direct indication of the velocity (or flow rate) of the moving material.

For several decades, devices based on this principle have found applications in a variety of fields, such as oceanography and medicine. More recently, electromagnetic flowmeters have become important in nuclear technology as devices for measuring the flow of radioactive fluids and, especially, the flow of liquid-metal coolants (such as Na,

*The work described herein was done at the Lewis Research Center as part of the NASA Summer Faculty Fellowship Program and at the Department of Electrical Engineering, City College of New York, under NASA Grant NGR-33-013-025 with Norman C. Wenger, Lewis Research Center, as Technical Monitor.

K, NaK, etc.) in the more advanced reactors and energy conversion devices. Satisfactory operation of these devices depends on the accurate measurement and control of the liquid-metal flow rates.

In addition to the stringent reliability requirements, many new problems arise in using electromagnetic flowmeters for measuring the flow rates of liquid metals because of their high temperatures and high electrical conductivities. As a result, interest in the design of electromagnetic flowmeters for liquid-metal applications has been renewed and their accurate calibration becomes important. Since many of the flowmeters used in the advanced reactors are quite large, it is preferable to compute a calibration curve for the flowmeters based on measured parameters of the flowmeter and the liquid metal rather than to perform an expensive and time-consuming experimental calibration of each flowmeter. The purpose of this study is to determine the relationship between the flowmeter output voltage and the parameters of the flowmeter and liquid metal so that these calibration curves can be computed.

The study will be restricted to the most common type of flowmeter used in liquid-metal applications. Figure 1 shows a cross-sectional view. The circular nonmagnetic pipe, situated in a uniform static magnetic field (between a pair of dc or permanent magnetic poles), is usually made of conducting materials (stainless steel, etc., for reasons of strength at high temperature and resistance to corrosion). Electrodes for detecting the output voltage are located at the two ends of a diameter, perpendicular to both the pipe axis and the magnetic field.

The motion of the liquid metal in the magnetic field causes a current to be induced in the liquid metal. This induced current reacts with the static magnetic field and produces a body force in the liquid metal which increases the pressure drop across the meter and distorts the velocity profile. In addition, the conducting pipe has a shunting effect on the output voltage.

Figure 2 shows a side view of the same electromagnetic flowmeter. The distortion of the applied magnetic field due to the end current loops, known as the magnetic edge effect, and the entrance length over which the full distortion of velocity profile by the magnetic field takes place can have an appreciable effect on the measured voltage. In this study, however, it will be assumed that the electromagnetic flowmeter is "long" so that the magnetic edges are far away from the electrodes and the velocity profile of the fluid has fully developed before passing through the electrodes.

Previous analytical and experimental studies of various types of electromagnetic flowmeters may be dated all the way back to Faraday's time. Williams (ref. 1) as early as 1930 analyzed the long circular dc electromagnetic flowmeter with nonconducting pipe walls. He showed that for some particular velocity distributions that are axially symmetric the potential difference at the outside edge of the stream is directly proportional to the average flow velocity and is independent of the electrical conductivity of the fluid. He verified his result in experiments with a copper sulfate solution and with mercury.

The general proof of this result for all axially symmetric velocity distributions was given by Kolin (ref. 2) in 1945. An exact mathematical solution of the circular flowmeter with nonconducting pipe walls has been obtained by Uflyand (ref. 3), Uhlenbusch and Fischer (ref. 4), and Gold (ref. 5) in the form of an infinite series involving modified Bessel functions of the first kind. These series converge very slowly, however, unless the Hartmann number M is small. Singh and Nariboli (ref. 6) obtained an asymptotic solution for large Hartmann numbers which converges rapidly for $M \geq 10$. All these results, however, are only valid for a flowmeter with nonconducting pipe walls.

Elrod and Fouse (ref. 7) in 1952 obtained an analytical result for a long circular dc electromagnetic flowmeter with conducting walls by assuming that the velocity profile is axially symmetric. Since then, their analytical result has been referenced in many theoretical discussions as well as forming the basis for comparison with much experimental data. Their result is not useful in making precision flow measurements in liquid metals, however, because they did not consider the distortion of the flow profile by the static magnetic field.

The most extensive studies, both theoretical and experimental, of the electromagnetic flowmeter have been made by Shercliff (refs. 8 to 10). His analytical solutions for long circular dc electromagnetic flowmeters with both nonconducting and conducting walls are also expressed in series form. These series converge very slowly except for values of M that are small ($M < 2.5$). He also obtained an approximate solution for the case where M is very large ($M > 100$) and the pipe walls are very thin. Unfortunately, this range of M does not cover most of the range encountered in practice and frequently the pipe walls are sufficiently thick so that the thin wall approximation is not valid.

The purpose of this study is to obtain solutions which are valid for all values of Hartmann number, fluid and wall conductivity, and pipe wall thickness. The approach to be used is to find the complete velocity and potential distributions in the fluid and in the pipe wall. From these distributions, the calibrations in terms of the ratio of the potential difference between the two electrodes to the mean velocity can be obtained. Since it is extremely difficult, if not impossible, to obtain the exact velocity and potential at every point inside the flowmeter in closed form, a numerical solution becomes a possible alternative. With the aid of high-speed computers, many two-dimensional problems have been solved successfully using numerical methods. For this reason, the long dc electromagnetic flowmeter which can be described by a two-dimensional model is being investigated initially. It is expected that the same numerical techniques developed from this study may be adopted successfully to study the case of dc electromagnetic flowmeters of finite length for which a more complicated three-dimensional model must be used.

THE MODEL

The model chosen for this study is a two-dimensional one, which applies to dc electromagnetic flowmeters of infinite length or long flowmeters in which the distorted velocity profile of the fluid has been fully developed into its ultimate shape before passing the electrodes. For convenience, as shown in figure 1, the applied magnetic field is assumed to be in the x-direction and the pipe axis coincides with the z-axis. The electrodes are located exactly at points B, C and A, D for the nonconducting and conducting pipe wall cases, respectively.

In this analysis, the following assumptions are made:

- (1) Steady state, incompressible, viscous fluid flow
- (2) Uniform static magnetic field
- (3) Magnetic permeability of fluid and pipe wall equal to that of free space
- (4) Homogeneous isotropic fluid and pipe wall conductivities
- (5) Fluid velocity in z-direction only (ref. 11), zero velocity at fluid and pipe wall interface
- (6) No electrical contact resistance at fluid and pipe wall interface
- (7) Negligible electric currents due to convection of charges by the fluid motion

BASIC EQUATIONS AND BOUNDARY CONDITIONS

The basic governing equations are derived from the following classic relations:

Modified Navier-Stokes equation for an incompressible fluid:

$$\rho_d(\vec{V} \cdot \nabla)\vec{V} = \eta \nabla^2 \vec{V} + \vec{J} \times \vec{B} - \nabla p \quad (1)$$

where ρ_d , η , p , \vec{V} , \vec{J} , and \vec{B} are the fluid density, viscosity, pressure, velocity, electric current density, and magnetic flux density, respectively. (Symbols are also defined in the appendix.)

Maxwell's equations:

$$\nabla \times \vec{E} = 0 \quad (2)$$

$$\nabla \times \vec{H} = \vec{J} \quad (3)$$

where \vec{E} and \vec{H} are electric and magnetic field intensity, respectively.

Ohm's law:

$$\vec{J} = \sigma_f(\vec{E} + \vec{V} \times \vec{B}) \quad (4)$$

where σ_f is the electrical conductivity of the fluid. From equation (2), the electric potential U is defined by

$$\vec{E} = -\nabla U \quad (5)$$

From equation (3)

$$\nabla \cdot \vec{J} = 0 \quad (6)$$

The flow velocity \vec{V} and the magnetic flux density \vec{B} can be expressed in component form as (see fig. 1)

$$\vec{V} = \hat{i}0 + \hat{j}0 + \hat{k}V_z = \hat{k}V_z \quad (7)$$

$$\vec{B} = \hat{i}B_o + \hat{j}0 + \hat{k}B_z = \hat{i}B_o + \hat{k}B_i \quad (8)$$

where B_o is the applied magnetic flux density and B_i is the magnetic flux density due to the induced current.

Substituting \vec{J} , \vec{V} , and \vec{B} from equations (4), (7), and (8) into equation (1) gives

$$\rho_d(\hat{k}V_z \cdot \nabla)\hat{k}V_z = \eta\hat{k}\nabla^2V_z + \sigma_f[-\nabla U + \hat{k}V_z \times (\hat{i}B_o + \hat{k}B_i)] \times (\hat{i}B_o + \hat{k}B_i) - \nabla p$$

The left-hand side of this equation reduces to zero. Thus

$$\eta\nabla^2V_z + \sigma_f B_o \left(\frac{\partial U}{\partial y} - V_z B_o \right) - \frac{\partial p}{\partial z} = 0 \quad (9)$$

becomes the first governing equation.

The second governing equation is obtained by combining equations (4) to (8), giving

$$\nabla^2 U = B_o \frac{\partial V_z}{\partial y} \quad (10)$$

For a two-dimensional model of a circular flowmeter, equations (9) and (10) are best written in cylindrical coordinates

$$\frac{\partial^2 V_z}{\partial r^2} + \frac{1}{r} \frac{\partial V_z}{\partial r} + \frac{1}{r^2} \frac{\partial^2 V_z}{\partial \theta^2} + \frac{\sigma_f B_o}{\eta} \left(\sin \theta \frac{\partial U}{\partial r} + \frac{\cos \theta}{r} \frac{\partial U}{\partial \theta} - V_z B_o \right) - \frac{1}{\eta} \frac{\partial p}{\partial z} = 0 \quad (11)$$

$$\frac{\partial^2 U}{\partial r^2} + \frac{1}{r} \frac{\partial U}{\partial r} + \frac{1}{r^2} \frac{\partial^2 U}{\partial \theta^2} - B_o \left(\sin \theta \frac{\partial V_z}{\partial r} + \frac{\cos \theta}{r} \frac{\partial V_z}{\partial \theta} \right) = 0 \quad (12)$$

Equations (11) and (12) can be made dimensionless by letting

$$\rho = \frac{r}{a}, \text{ dimensionless radius}$$

$$V = \frac{V_z}{V_o}, \text{ dimensionless velocity}$$

$$W = \frac{U}{B_o a V_o}, \text{ dimensionless potential}$$

$$k = - \frac{a^2}{\eta V_o} \frac{\partial p}{\partial z}, \text{ dimensionless pressure gradient}$$

$$M = B_o a \left(\frac{\sigma_f}{\eta} \right)^{1/2}, \text{ Hartmann number}$$

where V_o is a characteristic velocity of the fluid. The final forms of the two governing equations used in this study then become

$$\frac{\partial^2 V}{\partial \rho^2} + \frac{1}{\rho} \frac{\partial V}{\partial \rho} + \frac{1}{\rho^2} \frac{\partial^2 V}{\partial \theta^2} + M^2 \left(\sin \theta \frac{\partial W}{\partial \rho} + \frac{\cos \theta}{\rho} \frac{\partial W}{\partial \theta} - V \right) + k = 0 \quad (13)$$

$$\frac{\partial^2 W}{\partial \rho^2} + \frac{1}{\rho} \frac{\partial W}{\partial \rho} + \frac{1}{\rho^2} \frac{\partial^2 W}{\partial \theta^2} - \sin \theta \frac{\partial V}{\partial \rho} - \frac{\cos \theta}{\rho} \frac{\partial V}{\partial \theta} = 0 \quad (14)$$

Equations (13) and (14) form two coupled linear elliptic differential equations in the mutually dependent variables V and W . The solutions for V and W are directly proportional to the dimensionless pressure gradient k and implicitly related to the Hartmann

number M . Hence, the ratio of the potential difference between the electrodes to the mean velocity is independent of k but a function of M .

Equations (13) and (14) apply only in the fluid region. If the pipe wall is conductive, an additional equation must be introduced to describe the potential in the wall. This equation can be obtained from equation (14) by setting $V = 0$, giving

$$\frac{\partial^2 W}{\partial \rho^2} + \frac{1}{\rho} \frac{\partial W}{\partial \rho} + \frac{1}{\rho^2} \frac{\partial^2 W}{\partial \theta^2} = 0 \quad (15)$$

The boundary conditions at the fluid surface for the nonconducting wall case are

$$V|_{r=a^-} = 0 \quad (16)$$

and

$$\left. \frac{\partial W}{\partial \rho} \right|_{r=a^-} = 0 \quad (17)$$

For the conducting wall case, the boundary conditions at the fluid and wall interface are

$$V|_{r=a^-} = 0 \quad (16)$$

$$\left(\frac{\partial W}{\partial \theta} \right) \Big|_{r=a^-} = \left(\frac{\partial W}{\partial \theta} \right) \Big|_{r=a^+} \quad (18)$$

$$\sigma_f \left(\frac{\partial W}{\partial \rho} \right) \Big|_{r=a^-} = \sigma_w \left(\frac{\partial W}{\partial \rho} \right) \Big|_{r=a^+} \quad (19)$$

where σ_w is the electrical conductivity of the wall. At the outer surface of the conducting wall,

$$\left(\frac{\partial W}{\partial \rho} \right) \Big|_{r=b^-} = 0 \quad (20)$$

PREVIOUS RESULTS

Since the results by Elrod, Fouse, and Shercliff are widely known and have been used for comparison with many studies, theoretical as well as experimental, they are summarized here.

In obtaining their result for circular dc electromagnetic flowmeters, Elrod and Fouse (ref. 7) assumed that the velocity distribution is arbitrary but axially symmetric. Using the usual boundary conditions at the radii $r=a$ and $r=b$ (eqs. (18) to (20)), they solved equations (14) and (15) exactly. Their result expressed in terms of the flowmeter sensitivity is given by equation (21). (Flowmeter sensitivity is the ratio of the electric potential difference between points A and D, U_{AD} , to the product of the average flow velocity V_a , the pipe inner diameter $2a$, and the applied magnetic field strength B_o .)

$$\frac{U_{AD}}{B_o 2aV_a} = \frac{W_{AD}}{2V_m} = \frac{2R}{(1 - \gamma) + (1 + \gamma)R^2} \quad (21)$$

where $R = b/a$, $\gamma = \sigma_w/\sigma_f$, $V_m = V_a/V_o$ (the dimensionless mean fluid velocity), and $W_{AD} = U_{AD}/B_o aV_o$ (the dimensionless potential difference). For the nonconducting wall case ($\sigma_w = 0$).

$$\frac{U_{BC}}{B_o 2aV_a} = \frac{W_{BC}}{2V_m} = 1 \quad (22)$$

Shercliff has solved the governing equations without assuming an axially symmetric velocity profile. His results for small Hartmann number M are

Circular nonconducting wall case:

$$V_m = \frac{k}{8} \left(1 - \frac{M^2}{48} + \frac{7M^4}{9216} - \dots \right) \quad (23)$$

$$\frac{U_{BC}}{B_o 2aV_a} = \frac{W_{BC}}{2V_m} = \left(1 - \frac{M^2}{576} + \frac{47M^4}{921600} - \dots \right) \quad (24)$$

Circular conducting wall case:

$$V_m = \frac{k}{8} \left(1 - \frac{7 - 6\Gamma}{48} M^2 + \frac{199 - 336\Gamma + 144\Gamma^2}{9216} M^4 - \dots \right) \quad (25)$$

where $\Gamma = (1 + R^2)/[(1 - \gamma) + (1 + \gamma)R^2]$.

$$\frac{U_{AD}}{B_o 2aV_a} = \frac{W_{AD}}{2V_m} = C_1 \left(1 - C_2 M^2 + C_3 M^4 - \dots \right) \quad (26)$$

where

$$C_1 = \frac{2R}{(1 - \gamma) + (1 + \gamma)R^2}$$

$$C_2 = \frac{R^2}{576} \frac{(1 - \gamma) + (1 + \gamma)R^2}{(1 - \gamma) + (1 + \gamma)R^6}$$

$$C_3 = \frac{R^2}{921600} \frac{(1 - \gamma) + (1 + \gamma)R^2}{3[(1 - \gamma) + (1 + \gamma)R^6]} \left[185 - \frac{50(1 + R^6)}{(1 - \gamma) + (1 + \gamma)R^6} + 6R^2 \frac{(1 - \gamma) + (1 + \gamma)R^6}{(1 - \gamma) + (1 + \gamma)R^{10}} \right]$$

In equations (25) and (26) Shercliff computed only the terms up to M^2 . The author has extended the solution up to terms of M^4 . These series solutions converge very rapidly for small M and give results that are probably accurate to within 1 percent for $M < 2$.

Shercliff also obtained the following approximate solutions for high values of M :

Circular nonconducting wall case:

$$\frac{U_{BC}}{B_o 2aV_a} \doteq 0.926 \quad (27)$$

Circular thin conducting wall case:

$$\frac{U_{AD}}{B_o 2aV_a} \doteq C \quad (28)$$

where C is the dimensionless calibration or sensitivity which is a function of $(\sigma_w/\sigma_f)(b-a)M/a$ as shown in figure 3. According to Shercliff, equations (27) and (28) are accurate to within 1 percent for $M > 100$.

NUMERICAL METHOD

Of the numerical methods available for solving differential equations, the method of finite differences is more universally applicable and more frequently used than any other. When applying it to a two-dimensional problem, the area of interest is divided into fine meshes. The intersections of the mesh lines are called mesh points or nodes. The differential equation is replaced by a difference equation, where all derivatives are approximated by difference quotients over the mesh distances. By using the difference equation, the value of the solution at a given mesh point can be related to the values of the solution at neighboring points and at boundary points. This technique generates n algebraic equations involving a total of n unknowns, where n is the number of mesh points. The final solution of the difference equation is obtained by solving for the n unknowns. This is normally done by using an iterative process.

In this study, the solutions for V and W are obtained by the so-called "five-point" average formula, which is obtained by considering equations (13) to (15) in the general form of

$$\nabla^2 \phi(\rho, \theta) + \mathcal{F}(\rho, \theta) = 0 \quad (29)$$

Refer to figure 4; the derivatives in $\nabla^2 \phi(\rho, \theta)$ may be approximated in cylindrical coordinates at the point ρ_i, θ_i by the following (ref. 12):

$$\left. \begin{aligned} \frac{\partial^2 \phi}{\partial \rho^2} &\doteq \frac{1}{h^2} \frac{2}{\alpha(\alpha+1)} \left[\alpha \phi_b - (1+\alpha) \phi_i + \phi_a \right] \\ \frac{1}{\rho} \frac{\partial \phi}{\partial \rho} &\doteq \frac{1}{\rho_i \alpha(\alpha+1)h} \left[\phi_a - (1-\alpha^2) \phi_i - \alpha^2 \phi_b \right] \\ \frac{1}{\rho^2} \frac{\partial^2 \phi}{\partial \theta^2} &= \frac{1}{\rho_i^2 \delta^2} (\phi_r - 2\phi_i + \phi_l) \end{aligned} \right\} \quad (30)$$

where h and αh are adjacent radial mesh distances, and δ is the constant angular mesh distance. Substituting equation (30) into equation (29) gives

$$\frac{2}{\alpha(\alpha + 1)} \left[\left(1 + \frac{h}{2\rho_i}\right) \phi_a + \alpha \left(1 + \frac{\alpha h}{2\rho_i}\right) \phi_b \right] + \left(\frac{h}{\rho_i \delta}\right)^2 (\phi_l + \phi_r) - 2 \left[\frac{1}{\alpha} + \frac{h(1 - \alpha)}{2\alpha\rho_i} + \left(\frac{h}{\rho_i \delta}\right)^2 \right] \phi_i + h^2 \mathcal{F}(\rho_i, \theta_i) = 0 \quad (31)$$

To obtain the solution of this equation at each of the n mesh points, an iterative process known as the Gauss-Seidel method (ref. 13) is used. In this method the new value of ϕ_i at the mesh point i is obtained by solving equation (31) using the previous values of ϕ at the points a , b , r , and l , and the value of $\mathcal{F}(\rho, \theta)$ at the point i . The computed values of V and W have an error approaching zero as fast as h^2 or h , depending on whether a uniform radial mesh distance ($\alpha = 1$) or a variable radial mesh distance ($\alpha \neq 1$) is used.

In the nonconducting pipe wall case, the boundary conditions are satisfied at $r = a$ or $\rho_i = 1$ (see fig. 4) by letting $V_i = 0$ (eq. (16)) and $W_a = W_b$ (eq. (17)). Similarly, in the conducting wall case, the boundary conditions are satisfied at $r = a$ or $\rho_i = 1$ by letting $V_i = 0$ (eq. (16)) and at $r = b$ or $\rho_i = R$ by letting $W_a = W_b$ (eq. (20)). Boundary condition (18) is automatically satisfied since W_i is single valued on the boundary. The remaining boundary condition (eq. (19)) is usually handled by replacing equation (19) with a difference equation in the form of

$$\sigma_f \frac{W_i - W_b}{h_f} = \sigma_w \frac{W_a - W_i}{h_w}$$

where h_f and h_w are the mesh distances inside the fluid and pipe wall, respectively. However, the W_i obtained from this expression has an error approaching zero only as fast as h_f or h_w (ref. 12). To improve the accuracy at the boundary, an equivalent boundary condition given by equation (6) expressed in difference equation form is used instead of equation (19). The mesh size at the boundary is also reduced by a factor of 4 in computing W along the interface.

The exact procedure used in applying the method of finite differences to this problem is outlined as follows:

(1) Taking advantage of the fact that the velocity and potential distributions are symmetric about both x and y axes, solutions covering one quadrant of the pipe cross section only are computed. Mesh sizes of 20 to 26 radial points in the fluid plus eight radial points in the wall (if it is conductive) by 18 angular points were used in the computations.

(2) Initial values of velocity and potential are assigned to each mesh point according to some reasonable distribution function. For example, a parabolic velocity distribution is used for low M , or a distribution known to resemble the final solution is chosen for other values of M to save computer time.

(3) Since the calibration is independent of k , it is arbitrarily set equal to 1.

(4) The difference equation representing the first governing equation (eq. (13)) is solved first. The velocity at each mesh point in the fluid region is computed in a systematic order by using the latest values of the velocity and potential (from assumed initial value or step 5) at each mesh point as soon as they become available.

(5) Similarly, the difference equation representing the second governing equation (eq. (14)) is then solved for the potential at each mesh point in the fluid using the latest values of the potential and velocity (from step 4) available. Equation (15) is also solved in this step at each mesh point in the wall if the wall is conductive.

(6) Completion of procedures 4 and 5 once is called one iteration. This iteration process is repeated until the fractional difference between two successive iterated results falls below a certain cutoff value. In obtaining the final results, a cutoff value of 10^{-5} is used for V_m , W_{BC} (or W_{AD}), and $W_{BC}/2V_m$ (or $W_{AD}/2V_m$).

The main concerns in using the numerical method are the attainable accuracy and the computation time required. Usually the accuracy can be improved by dividing the area of interest into finer meshes, thus increasing the number of mesh points. However, this will also increase the number of equations to be solved, and the computation time required will increase in an even greater proportion. For the low Hartmann number cases ($M \leq 2$), uniformly spaced ($\alpha = 1$) radial mesh points were used (20 radial by 18 angular for the nonconductive wall and (20 + 8) radial by 18 angular for the conductive wall). These mesh sizes correspond to 362 simultaneous equations for velocity and 360 or 504 simultaneous equations for potential in the nonconducting or conducting pipe wall cases, respectively.

For higher Hartmann numbers, the velocity profile consists of a core of almost uniform velocity and a thin boundary layer where the velocity drops rapidly from its core value to zero at the wall (ref. 10). In order to describe the velocity gradient near the pipe wall more accurately, gradually reduced radial mesh distances ($\alpha < 1$) are used. The best values of these radial mesh sizes are determined by "trial and error" using the nonconducting wall case as a check, since the center velocity for different Hartmann numbers in this case can be calculated exactly (refs. 3 to 5). For $M \geq 5$, variable mesh sizes up to 26 radial points by 18 angular points for the nonconducting wall case and (26 + 8) radial points by 18 angular points for the conducting wall case were used and found to be satisfactory.

To decrease the required computer time the successive overrelaxation method (S O R) was used. This method is valid in this case because the coefficient matrix of the algebraic equations to be solved possesses the so-called property "A" (ref. 14). In this

method, the value obtained from equation (31) for the q^{th} iteration $\phi_i^{(q)}$ is modified with a larger anticipated change by the relation

$$\phi_i^{(q)*} = \omega \phi_i^{(q)} - (\omega - 1) \phi_i^{(q-1)} \quad (32)$$

where $\phi_i^{(q)*}$ is the new value for mesh point i resulting from q^{th} iteration and ω is called the accelerating factor. The rate of convergence in using the S O R method depends on the value of ω chosen. Since there is no formula for calculating the best value of ω in cylindrical geometry, its value must be obtained by testing and estimation. It was found that the best value of ω is independent of Hartmann number M and varies only slightly when the mesh size is changed. The values of ω chosen for the nonconducting and conducting wall cases are 1.91 and 1.93, respectively. To avoid any "overshoot," the S O R method is dropped by letting $\omega = 1$ (Gauss-Seidel) when the velocity and potential distributions are approaching their final shape near the end of each computer run.

RESULTS

Numerical solutions for the velocity and potential distributions inside a circular electromagnetic flowmeter were obtained for both the nonconducting and conducting wall cases over the range of Hartmann number, $M = 1$ to $M = 200$. In the conducting wall case, the conductivity and radius ratios used were $\sigma_w/\sigma_f = 0.1, 0.5, 1.0, 1.5, 2.0$; and $b/a = 1.05, 1.15, 1.25, 1.35$. These values cover the usual materials and pipe sizes commonly used in the liquid-metal flow rate measurements. Typical results are presented in graphical form.

Figures 5 to 9 show velocity profiles at $\theta = 0^\circ, 30^\circ, 60^\circ, \text{ and } 90^\circ$ (θ is measured with respect to the applied magnetic field B_o or x -axis, see fig. 1) inside the flowmeter for different values of Hartmann number M . Five cases are shown: (1) nonconducting pipe wall; (2) $\sigma_w/\sigma_f = 0.1, b/a = 1.05$; (3) $\sigma_w/\sigma_f = 0.1, b/a = 1.35$; (4) $\sigma_w/\sigma_f = 2.0, b/a = 1.05$; and (5) $\sigma_w/\sigma_f = 2.0, b/a = 1.35$. The velocity profiles are normalized with respect to the dimensionless mean velocity V_m .

Velocity contour diagrams for the same cases are also shown in figures 10 to 14. The velocity contours are normalized with respect to the dimensionless center velocity V_c . The figures are arranged in increasing order of the quantity $[(b/a) - 1] \sigma_w/\sigma_f$ to observe the effect of thicker and more highly conductive pipe walls on the velocity profiles.

It is quite obvious for the nonconducting wall case that the velocity profile is more flattened along the x -axis ($\theta = 0^\circ$) than along the y -axis ($\theta = 90^\circ$) due to the body force

created by the induced current. Therefore the assumption of axially symmetry in the velocity profile is not valid, especially when the Hartmann number M is large.

The effect of the conducting wall on the velocity profile may be observed by comparing these figures. In the case of $\sigma_w/\sigma_f = 0.1$ and $b/a = 1.05$ (fig. 6), the effect is small at least for M values up to 100 since the wall conductivity and thickness are small. The resulting velocity profiles for this case resemble more those in the nonconducting wall case (fig. 5). As the quantity $[(b/a) - 1] \sigma_w/\sigma_f$ increases (figs. 6 to 9), the effect of the wall becomes quite pronounced. For the thickest, most highly conductive, wall case considered (fig. 9) the maximum velocity is only 5 percent higher than the average velocity when M is 100. The velocity profile for this case is essentially that of slug flow when M is large.

Figures 15 to 17 show the potential distribution along the y -axis for the nonconducting wall case and two conducting wall cases ($\sigma_w/\sigma_f = 0.1$, $b/a = 1.05$ and $\sigma_w/\sigma_f = 2.0$, $b/a = 1.35$). Since the electrodes at B, C and A, D are located along the y -axis, these distributions determine the total potential difference between the electrodes. It is quite clear that the potential distributions in a poorly conducting wall case (σ_w/σ_f , $b/a = 1.05$, fig. 16) resemble those in the nonconducting wall case (fig. 15) and are less affected by the Hartmann number at least for $M \leq 100$ than those in the highly conducting wall case (fig. 17). However, in both conducting cases, the maximum potential occurs inside the fluid rather than on the fluid and wall interface or inside the pipe wall. This is in full agreement with the boundary condition (eq. (19)). Since there is no source for the induced potential inside the conducting pipe wall, the potential gradient across the boundary is negative.

Calibration curves giving the ratio of the dimensionless potential difference to the dimensionless mean flow velocity ($W_{BC}/2V_m$ and $W_{AD}/2V_m$) as functions of Hartmann number M for all cases studied are presented in figures 18 to 22. The same results also appear in tabular form in table I.

For small M the calibration curves agree with the results of Elrod and Fouse (eq. (21)) and Shercliff (eq. (26)) for the conducting wall cases, and with the result of Gold (ref. 5) over a much larger range of M for the nonconducting wall case. As M increases the calibration curves initially decrease; and if the pipe wall is nonconductive, the curve becomes asymptotic to about 0.93 as M becomes infinite (fig. 18). However, if the pipe wall is conductive, the curves reach a minimum in the M range of 10 to 50 and then increase with increasing M and become asymptotic to their initial value at $M = 0$ as M becomes infinite.

The reason for this behavior can be seen by examining the velocity profiles. First, consider the velocity profile for a thick highly conductive pipe wall which is shown in figure 9. The velocity profile is axially symmetric in the limit of both very high and very low M . For very low M the profile is parabolic, and for very high M the profile

approximates that of slug flow. Thus, the solution of Elrod and Fouse, which holds only for symmetric profiles, can be used for the limit of high and low M and the same result will be obtained.

It is known from the general theory of magnetohydrodynamic channel flow (ref. 15) that the velocity profile also approximates that of slug flow in the limit as M becomes infinite even if the pipe walls are thin and less conductive. However, it takes a much larger value of M to achieve this condition if the walls are thin or of low conductivity than if they are thick and highly conductive. This effect can be observed by comparing figures 5 to 9. Even at $M = 100$ the velocity profile for the thinnest, least conductive wall case considered (fig. 6) resembles that of the nonconductive pipe wall. Nevertheless, as M is increased, this velocity profile will eventually approach that of slug flow. Thus, for all conductive pipe wall cases, each calibration curve in the limit as M becomes infinite will approach its value at $M = 0$.

The results for the nonconductive pipe wall are quite different. The velocity profile for this case, shown in figure 5, does not approach that of slug flow as M becomes infinite. This is also born out by the general theory of magnetohydrodynamic channel flow (ref. 15). Consequently, the calibration curve does not recover to its value at $M = 0$ but continually decreases as M becomes large and becomes asymptotic to about 0.93 as M becomes infinite. This is in agreement with the value computed by Gold (ref. 5) and Shercliff (refs. 8 to 10) of 0.925.

A rather difficult task in this study is to estimate the accuracy of the calibration results. First, the accuracy is limited by the accuracy of the model and the governing equations. Secondly, it depends on the cumulative accuracies of the computed velocity and potential values at all mesh points. Commonly, the error of a value obtained at each mesh point may be divided into two parts, such as,

$$\text{Error} = (S - N) = (S - s) + (s - N) \quad (33)$$

where S is the exact solution of the partial differential equation and s and N are the exact and computed solutions of the difference equation, respectively. The quantity $(S - s)$ is the discretization error and $(s - N)$ is the stability error. The discretization error, in general, can be reduced by increasing the number of mesh points. It is limited only by such factors as computer time and storage. However, the exact expression for the discretization error is given in terms of unknown derivatives for which no upper and lower bounds can be found (ref. 14). To find its approximate effect on the final results, calculations were carried out for various mesh sizes with all other conditions the same. Using the nonconducting wall case at $M = 100$ and 10^{-5} cutoff as an example, the results are as follows:

Mesh size		$W_{BC}/2V_m$
Number of radial points	Number of angular points	
15	18	0.93122
26	18	.93206
30	36	.93261

Changes of the same order of magnitude were also found for a few selected conducting wall cases. To save computer time, maximum mesh sizes of 26 radial points by 18 angular points and (26 + 8) radial points by 18 angular points were selected to obtain final results for the nonconducting and conducting wall cases, respectively.

The stability error ($s - N$) may be divided into the "roundoff" and the "cutoff" errors. The roundoff error arises from the finite number of significant figures used to perform the arithmetic operations. This error can cause instability if it is allowed to accumulate in an iterative process. The cutoff error depends on the cutoff level at which the iteration process is terminated.

The stability error is a computational error and usually it is not possible to determine its magnitude. However, for the results obtained from this study, the stability error should be quite small for two reasons. First, the roundoff error should be small since all computer runs were carried out in double precision (15 significant figures) and the total number of iterations never exceeded 4000. Secondly, the cutoff value, which terminates the calculation if the fractional difference between two successive iterations falls below it, was set at 10^{-5} for all results. Tests have shown that the improvement in accuracy by lowering the cutoff value usually is not worth the extra computer time. As an illustration, for the case of $\sigma_w/\sigma_f = 0.5$, $b/a = 1.05$, and $M = 100$, the ratios of $W_{AD}/2V_m$ obtained for various cutoff values are as follows:

Cutoff value	Number of iterations	$W_{AD}/2V_m$
10^{-5}	1217	0.92881
10^{-6}	2863	.92821
10^{-7}	4512	.92812

It is obvious in this case, that it is not worthwhile to use cutoff value less than 10^{-5} .

CONCLUDING REMARKS

The numerical method of finite differences has been used to determine the complete velocity and potential distributions inside a long dc electromagnetic flowmeter for both nonconducting and conducting pipe wall cases. In the measurement of liquid-metal flow rates, the velocity profile is distorted due to the body force created by the induced current and the applied magnetic field. The assumption of an axially symmetric velocity profile was shown to be not valid for many cases especially when the Hartmann number is large. The calibration results obtained from this study may be used to correct flow measurements for the effect of velocity profile distortion. The results are based on the assumption that the electromagnetic flowmeter is sufficiently long so that the velocity profile is fully developed. For short electromagnetic flowmeters, in which the entrance and magnetic edge effects must be included, a more complicated three-dimensional study will be required.

Lewis Research Center,
National Aeronautics and Space Administration,
Cleveland, Ohio, May 18, 1971,
128-31

APPENDIX - SYMBOLS

a	inner radius of flowmeter pipe
\vec{B}	magnetic flux density
\vec{B}_i, \vec{B}_o	induced and applied magnetic flux density, respectively
b	outer radius of flowmeter pipe
C	calibration or sensitivity used in fig. 3, $U_{AD}/B_o 2aV_a$
C_1, C_2, C_3	parameters in eq. (26)
\vec{E}	electric field intensity
\vec{H}	magnetic field intensity
h	radial mesh distance
h_f, h_w	radial mesh distances inside fluid and pipe wall, respectively
$\hat{i}, \hat{j}, \hat{k}$	unit vectors along x, y, z coordinate axes
\vec{J}	electric current density
k	dimensionless pressure gradient, $-\frac{a^2}{\eta V_o} \frac{\partial p}{\partial z}$
M	Hartmann number, $B_o a (\sigma/\eta)^{1/2}$
N	computed solution of difference equation
n	total number of mesh points
p	pressure inside fluid
R	ratio of outer-to-inner pipe radii, b/a
r	radial distance
S	exact solution of differential equation
s	exact solution of difference equation
U	electric potential
U_{AD}	electric potential difference between electrodes A and D
U_{BC}	electric potential difference between electrodes B and C
V	dimensionless fluid velocity in z-direction, V_z/V_o
\vec{V}	fluid velocity vector
V_a	mean fluid velocity
V_c	dimensionless fluid velocity at center of pipe

V_m	dimensionless mean fluid velocity, V_a/V_o
V_o	characteristic velocity of fluid
V_z	fluid velocity in z-direction
W	dimensionless electric potential, $U/B_o aV_o$
W_{AD}	dimensionless potential difference between electrodes A and D, $U_{AD}/B_o aV_o$
W_{BC}	dimensionless potential difference between electrodes B and C, $U_{BC}/B_o aV_o$
x, y, z	Cartesian coordinates
α	ratio of adjacent radial mesh distances
Γ	parameter used in eq. (25), $(1 + R^2)/[(1 - \gamma) + (1 + \gamma)R^2]$
γ	ratio of wall-to-fluid conductivity, σ_w/σ_f
δ	angular mesh distance
η	viscosity of fluid
θ	angular variable
ρ	dimensionless radial distance, r/a
ρ_d	fluid density
σ_f, σ_w	electric conductivity of fluid and pipe wall, respectively
ϕ	arbitrary function of ρ and θ
ω	accelerating factor used in S O R method

REFERENCES

1. Williams, E. J.: The Induction of Electromotive Forces In a Moving Liquid by a Magnetic Field, and Its Application to an Investigation of the Flow of Liquids. Proc. Phys. Soc. (London), vol. 42, pt. 5, no. 235, Aug. 15, 1930, pp. 466-478.
2. Kolin, Alexander: An Alternating Field Induction Flow Meter of High Sensitivity. Rev. Sci. Inst., vol. 16, no. 5, May 1945, pp. 109-116.
3. Uflyand, Ya. S.: Hartman Problem for a Circular Tube. Soviet Phys. - Tech. Phys., vol. 5, no. 10, Apr. 1961, pp. 1194-1196.
4. Uhlenbusch, J.; and Fischer, E.: Hydromagnetische Strömung im kreiszylindrischen Rohr. Zeit. f. Physik, vol. 164, Aug. 3, 1961, pp. 190-198.
5. Gold, Richard R.: Magnetohydrodynamic Pipe Flow. Part 1. J. Fluid Mech., vol. 13, pt. 4, Aug. 1962, pp. 505-512.
6. Singh, S. N.; and Nariboli, G. A.: Asymptotic Solution for the Hartmann Problem Through Circular Tube. Appl. Sci. Res., Sec. B, vol. 11, 1964, pp. 145-160.
7. Elrod, H. G., Jr.; and Fouse, R. R.: An Investigation of Electromagnetic Flowmeters. Trans. ASME, vol. 74, no. 4, May 1952, pp. 589-594.
8. Shercliff, J. A.: The Theory of the D.C. Electromagnetic Flowmeter for Liquid Metals. Rep. AERE-X/R-1052, Atomic Energy Research Establishment, 1952.
9. Shercliff, J. A.: The Flow of Conducting Fluids in Circular Pipes Under Transverse Magnetic Fields. J. Fluid Mech., vol. 1, pt. 6, Dec. 1956, pp. 644-666.
10. Shercliff, J. A.: The Theory of Electromagnetic Flow-Measurement. Cambridge Univ. Press, 1962.
11. Maslen, Stephen H.: Transverse Velocities in Fully Developed Flows. Quart. Appl. Math., vol. 16, no. 2, July 1958.
12. Salvadori, Mario G.; and Baron, Melvin L.: Numerical Methods in Engineering. Prentice-Hall, Inc., 1959.
13. Varga, Richard S.: Matrix Iterative Analysis. Prentice-Hall, Inc., 1962.
14. Smith, Gordon D.: Numerical Solution of Partial Differential Equations. Oxford University Press, 1965.
15. Chang, Chieh C.; and Lundgren, Thomas S.: Duct Flow in Magnetohydrodynamics. Zeit. f. Angew. Math. Phys., vol. 12, 1961, pp. 100-114.

TABLE I. - CALIBRATION FOR dc ELECTROMAGNETIC FLOWMETER

Hartmann number, M	Dimensionless mean fluid velocity, V_m	Dimensionless potential, W_{AD}	Ratio, $W_{AD}/2V_m$	Hartmann number, M	Dimensionless mean fluid velocity, V_m	Dimensionless potential, W_{AD}	Ratio, $W_{AD}/2V_m$
Nonconducting pipe wall ^a , $\sigma_w/\sigma_f = 0$				$b/a = 1.15$, $\sigma_w/\sigma_f = 0.1$			
1	0.123	0.244	0.997	1	0.122	0.239	0.976
2	.116	.230	.992	2	.115	.224	.972
5	$.892 \times 10^{-1}$.174	.975	5	$.865 \times 10^{-1}$.165	.955
10	.603	.115	.956	10	.556	.104	.939
20	.352	$.662 \times 10^{-1}$.940	20	.294	$.546 \times 10^{-1}$.927
50	.154	.288	.934	50	.101	.187	.925
100	$.799 \times 10^{-2}$.149	.932	100	$.377 \times 10^{-2}$	$.698 \times 10^{-2}$.925
200	.409	$.768 \times 10^{-2}$.932	200	.125	.231	.926
$b/a = 1.05$, $\sigma_w/\sigma_f = 0.1$				$b/a = 1.15$, $\sigma_w/\sigma_f = 0.5$			
1	0.122	0.243	0.993	1	0.122	0.225	0.925
2	.116	.228	.988	2	.112	.207	.922
5	$.882 \times 10^{-1}$.171	.970	5	$.779 \times 10^{-1}$.141	.908
10	.585	.111	.951	10	.431	$.773 \times 10^{-1}$.896
20	.329	$.617 \times 10^{-1}$.937	20	.183	.325	.891
50	.130	.242	.929	50	$.441 \times 10^{-2}$	$.791 \times 10^{-2}$.898
100	$.573 \times 10^{-2}$.106	.928	100	.130	.235	.904
200	.212	$.395 \times 10^{-2}$.929	200	$.347 \times 10^{-3}$	$.631 \times 10^{-3}$.909
$b/a = 1.05$, $\sigma_w/\sigma_f = 0.5$				$b/a = 1.15$, $\sigma_w/\sigma_f = 1.0$			
1	0.122	0.238	0.973	1	0.121	0.210	0.869
2	.114	.222	.969	2	.110	.190	.866
5	$.846 \times 10^{-1}$.165	.952	5	$.701 \times 10^{-1}$.120	.854
10	.524	$.981 \times 10^{-1}$.936	10	.346	$.585 \times 10^{-1}$.846
20	.261	.483	.925	20	.129	.217	.845
50	$.816 \times 10^{-2}$.151	.925	50	$.270 \times 10^{-2}$	$.461 \times 10^{-2}$.852
100	.280	$.520 \times 10^{-2}$.929	100	$.745 \times 10^{-3}$.128	.859
200	$.835 \times 10^{-3}$.156	.934	200	.196	$.338 \times 10^{-3}$.862
$b/a = 1.05$, $\sigma_w/\sigma_f = 1.0$				$b/a = 1.15$, $\sigma_w/\sigma_f = 1.5$			
1	0.122	0.231	0.951	1	0.120	0.196	0.819
2	.113	.215	.947	2	.107	.175	.817
5	$.806 \times 10^{-1}$.150	.931	5	$.644 \times 10^{-1}$.104	.807
10	.470	.862	.918	10	.294	$.470 \times 10^{-1}$.800
20	.212	.386	.911	20	.102	.163	.800
50	$.555 \times 10^{-2}$	$.102 \times 10^{-1}$.916	50	$.201 \times 10^{-2}$	$.326 \times 10^{-2}$.808
100	.171	$.315 \times 10^{-2}$.919	100	$.540 \times 10^{-3}$	$.878 \times 10^{-3}$.813
200	$.483 \times 10^{-3}$	$.896 \times 10^{-3}$.927	200	.142	.232	.815
$b/a = 1.05$, $\sigma_w/\sigma_f = 1.5$				$b/a = 1.15$, $\sigma_w/\sigma_f = 2.0$			
1	0.121	0.226	0.930	1	0.119	0.185	0.775
2	.112	.208	.925	2	.105	.163	.772
5	$.770 \times 10^{-1}$.140	.909	5	$.600 \times 10^{-1}$	$.917 \times 10^{-1}$.764
10	.425	$.764 \times 10^{-1}$.899	10	.259	.394	.759
20	.179	.320	.895	20	$.860 \times 10^{-2}$.131	.760
50	$.427 \times 10^{-2}$	$.771 \times 10^{-2}$.902	50	.164	$.252 \times 10^{-2}$.767
100	.125	.228	.909	100	$.433 \times 10^{-3}$	$.668 \times 10^{-3}$.771
200	$.334 \times 10^{-3}$	$.611 \times 10^{-3}$.913	200	.111	.172	.773
$b/a = 1.05$, $\sigma_w/\sigma_f = 2.0$				$b/a = 1.25$, $\sigma_w/\sigma_f = 0.1$			
1	0.121	0.220	0.910	1	0.122	0.233	0.954
2	.111	.202	.906	2	.115	.218	.950
5	$.745 \times 10^{-1}$.133	.893	5	$.851 \times 10^{-1}$.159	.936
10	.391	$.690 \times 10^{-1}$.882	10	.532	$.982 \times 10^{-1}$.922
20	.156	.273	.879	20	.269	.492	.913
50	$.350 \times 10^{-2}$	$.621 \times 10^{-2}$.886	50	$.845 \times 10^{-2}$.154	.913
100	$.995 \times 10^{-3}$.178	.893	100	.293	$.537 \times 10^{-2}$.917
200	.267	$.479 \times 10^{-3}$.898	200	$.906 \times 10^{-3}$.167	.920

^aValues shown for potential and ratio are W_{BC} and $W_{BC}/2V_m$, respectively.

TABLE I. - Concluded. CALIBRATION FOR dc ELECTROMAGNETIC FLOWMETER

Hartmann number, M	Dimensionless mean fluid velocity, V_m	Dimensionless potential, W_{AD}	Ratio, $W_{AD}/2V_m$	Hartmann number, M	Dimensionless mean fluid velocity, V_m	Dimensionless potential, W_{AD}	Ratio, $W_{AD}/2V_m$
$b/a = 1.25, \sigma_w/\sigma_f = 0.5$				$b/a = 1.35, \sigma_w/\sigma_f = 1.0$			
1	0.121	0.213	0.878	1	0.119	0.177	0.741
2	.111	.194	.876	2	.105	.155	.739
5	$.730 \times 10^{-1}$.126	.864	5	$.593 \times 10^{-1}$	$.868 \times 10^{-1}$.732
10	.376	$.643 \times 10^{-1}$.856	10	.254	.370	.728
20	.146	.249	.853	20	$.837 \times 10^{-2}$.122	.729
50	$.320 \times 10^{-2}$	$.551 \times 10^{-2}$.861	50	.159	$.233 \times 10^{-2}$.735
100	$.900 \times 10^{-3}$.156	.867	100	$.419 \times 10^{-3}$	$.619 \times 10^{-3}$.739
200	.236	$.410 \times 10^{-3}$.870	200	.107	.159	.741
$b/a = 1.25, \sigma_w/\sigma_f = 1.0$				$b/a = 1.35, \sigma_w/\sigma_f = 1.5$			
1	0.120	0.192	0.800	1	0.118	0.157	0.666
2	.107	.170	.797	2	.102	.135	.664
5	$.636 \times 10^{-1}$.100	.789	5	$.531 \times 10^{-1}$	$.670 \times 10^{-1}$.659
10	.287	$.450 \times 10^{-1}$.783	10	.212	.278	.656
20	$.988 \times 10^{-2}$.155	.783	20	$.662 \times 10^{-2}$	$.870 \times 10^{-2}$.657
50	.194	$.307 \times 10^{-2}$.790	50	.121	.160	.662
100	$.518 \times 10^{-3}$	$.824 \times 10^{-3}$.795	100	$.314 \times 10^{-3}$	$.418 \times 10^{-3}$.665
200	.134	.214	.798	200	$.801 \times 10^{-4}$.107	.667
$b/a = 1.25, \sigma_w/\sigma_f = 1.5$				$b/a = 1.35, \sigma_w/\sigma_f = 2.0$			
1	0.119	0.174	0.734	1	0.117	0.142	0.605
2	.104	.152	.732	2	$.989 \times 10^{-1}$.119	.603
5	$.574 \times 10^{-1}$	$.832 \times 10^{-1}$.725	5	.489	$.586 \times 10^{-1}$.599
10	.240	.346	.721	10	.186	.222	.597
20	$.779 \times 10^{-2}$.112	.722	20	$.565 \times 10^{-2}$	$.676 \times 10^{-2}$.598
50	.146	$.212 \times 10^{-2}$.728	50	.101	.122	.602
100	$.382 \times 10^{-3}$	$.560 \times 10^{-3}$.732	100	$.261 \times 10^{-3}$	$.316 \times 10^{-3}$.605
200	$.980 \times 10^{-4}$.144	.734	200	$.663 \times 10^{-4}$	$.803 \times 10^{-4}$.606
$b/a = 1.25, \sigma_w/\sigma_f = 2.0$							
1	0.118	0.160	0.678				
2	.101	.137	.676				
5	$.530 \times 10^{-1}$	$.710 \times 10^{-1}$.670				
10	.211	.281	.667				
20	$.659 \times 10^{-2}$	$.881 \times 10^{-2}$.668				
50	.120	.162	.674				
100	$.313 \times 10^{-3}$	$.423 \times 10^{-3}$.677				
200	$.795 \times 10^{-4}$.108	.678				
$b/a = 1.35, \sigma_w/\sigma_f = 0.1$							
1	0.122	0.227	0.929				
2	.114	.212	.926				
5	$.839 \times 10^{-1}$.153	.914				
10	.514	$.927 \times 10^{-1}$.902				
20	.251	.449	.895				
50	$.738 \times 10^{-2}$.132	.897				
100	.244	$.440 \times 10^{-2}$.901				
200	$.728 \times 10^{-3}$.132	.904				
$b/a = 1.35, \sigma_w/\sigma_f = 0.5$							
1	0.121	0.201	0.835				
2	.109	.182	.832				
5	$.695 \times 10^{-1}$.114	.823				
10	.339	$.554 \times 10^{-1}$.817				
20	.125	.204	.816				
50	$.261 \times 10^{-2}$	$.429 \times 10^{-2}$.822				
100	$.716 \times 10^{-3}$.119	.828				
200	.187	$.311 \times 10^{-3}$.831				

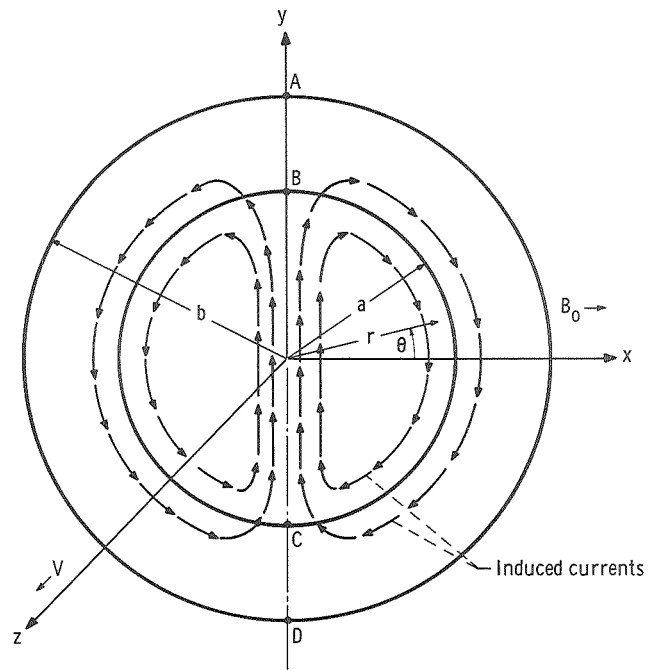


Figure 1. - Cross-sectional view of circular dc electromagnetic flowmeter.

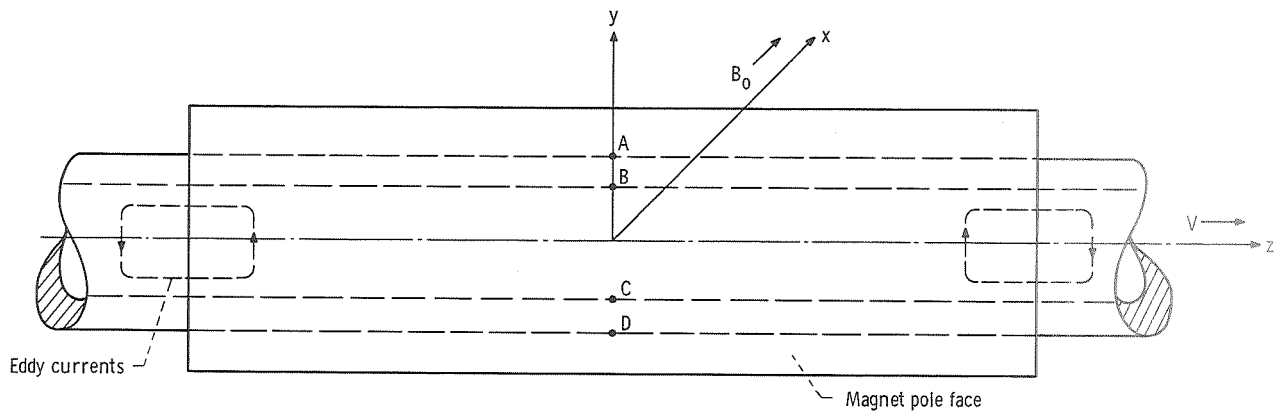


Figure 2. - Side view of circular dc electromagnetic flowmeter.

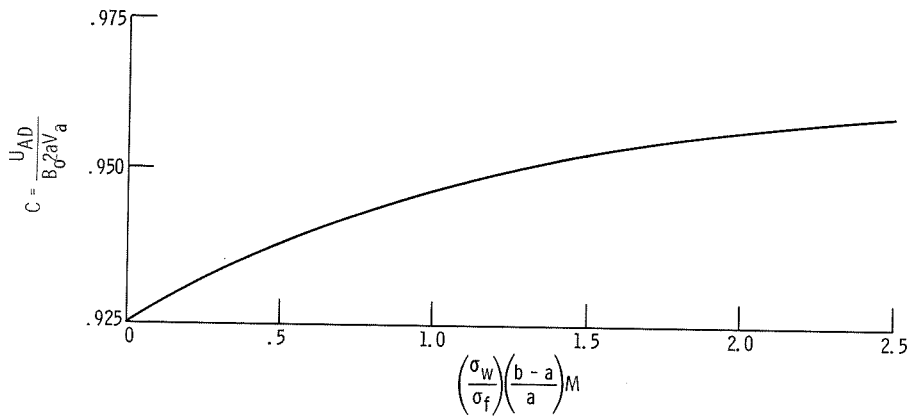


Figure 3. - Effect of wall conductivity on sensitivity at high Hartmann number M . (From refs. 8 and 10, Shercliff.)

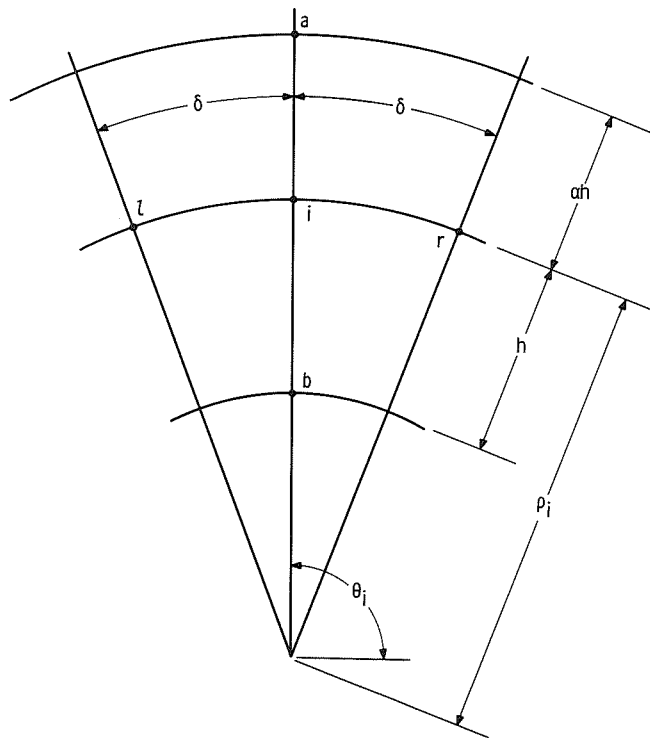


Figure 4. - Typical lattice used in "five-point" average method.

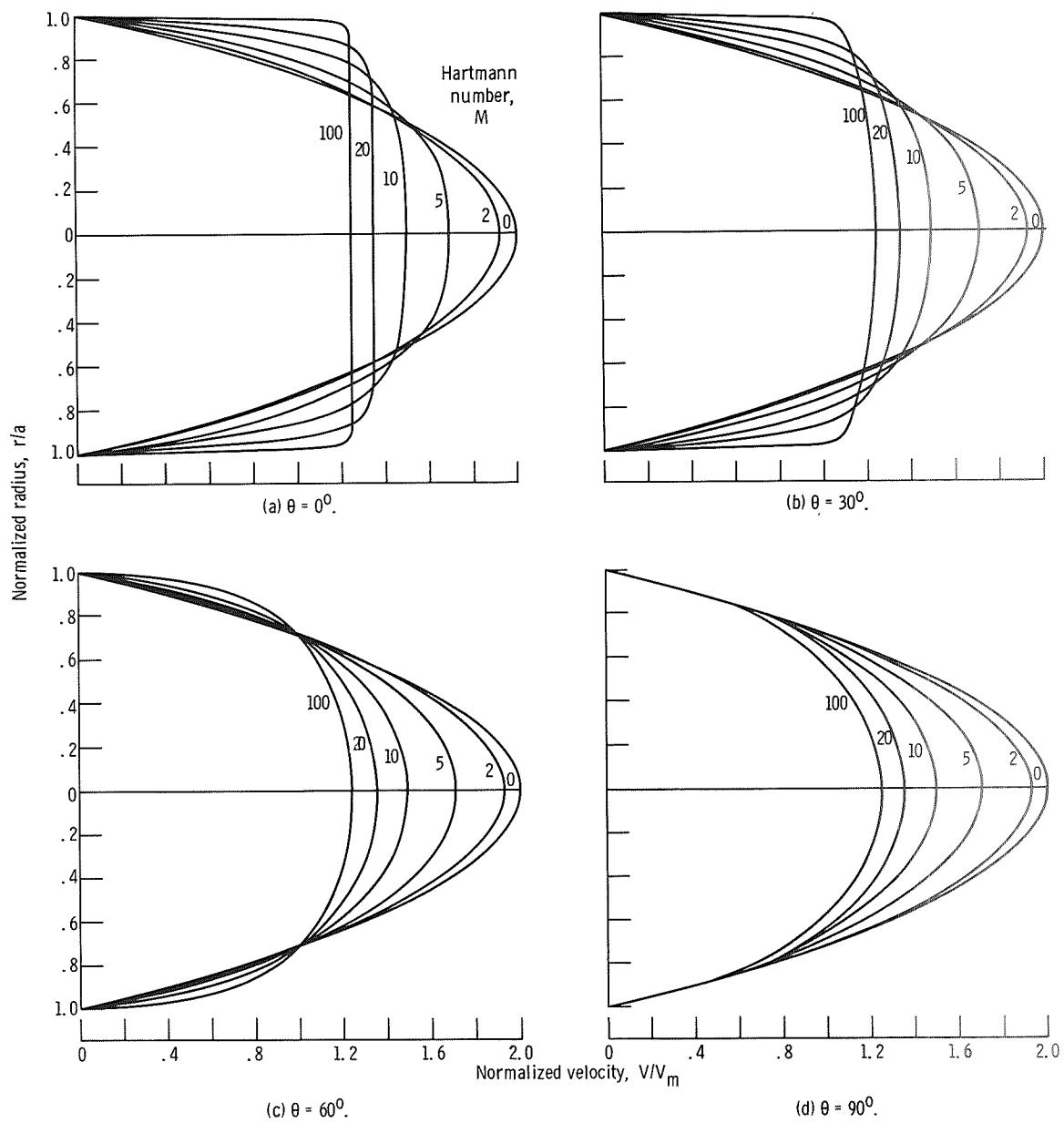


Figure 5. - Normalized velocity profiles for nonconducting wall.

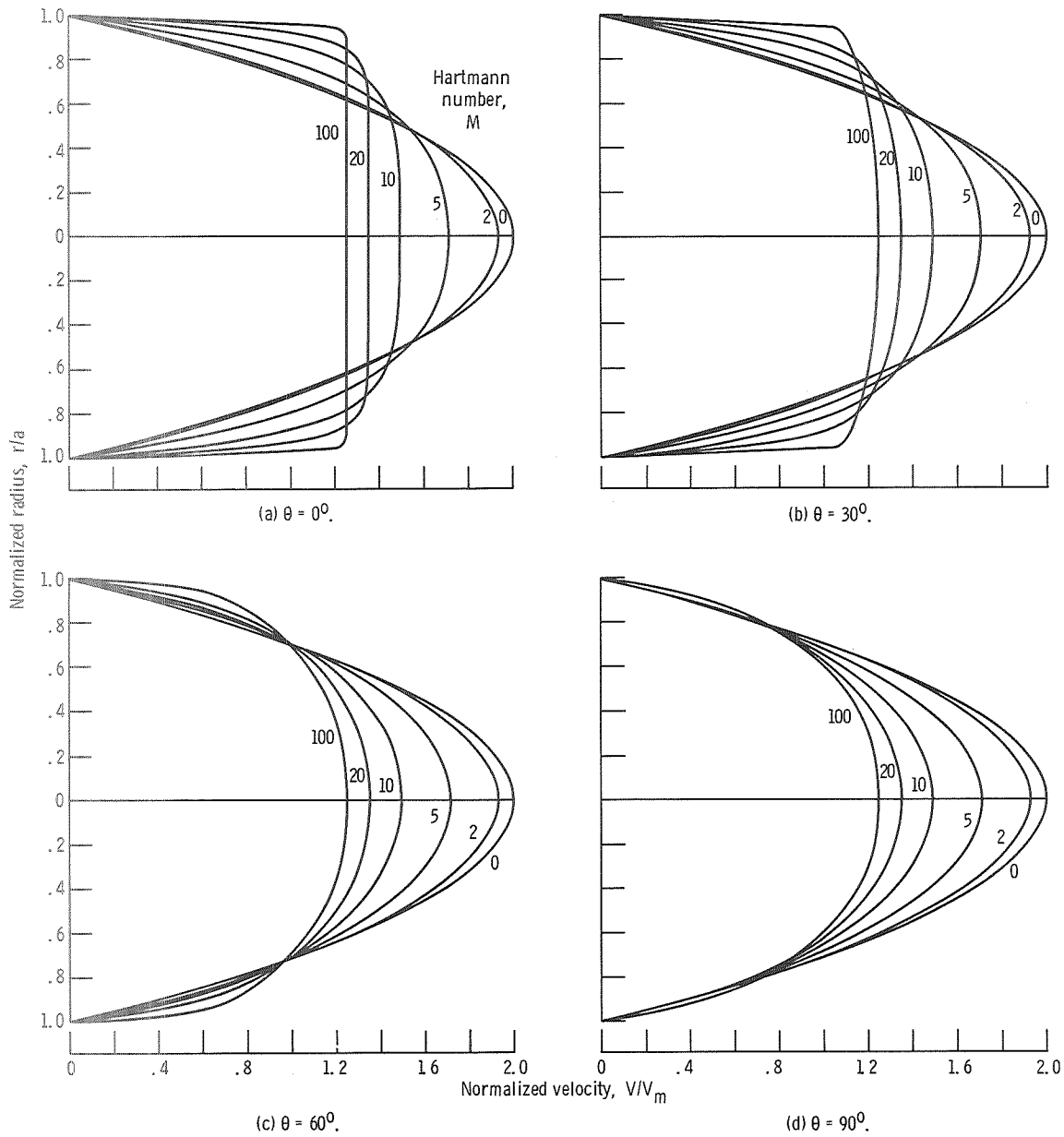


Figure 6. - Normalized velocity profiles for conducting wall with wall-to-fluid electrical conductivity ratio σ_w/σ_f of 0.1 and flowmeter pipe outer-to-inner radius ratio b/a of 1.05.

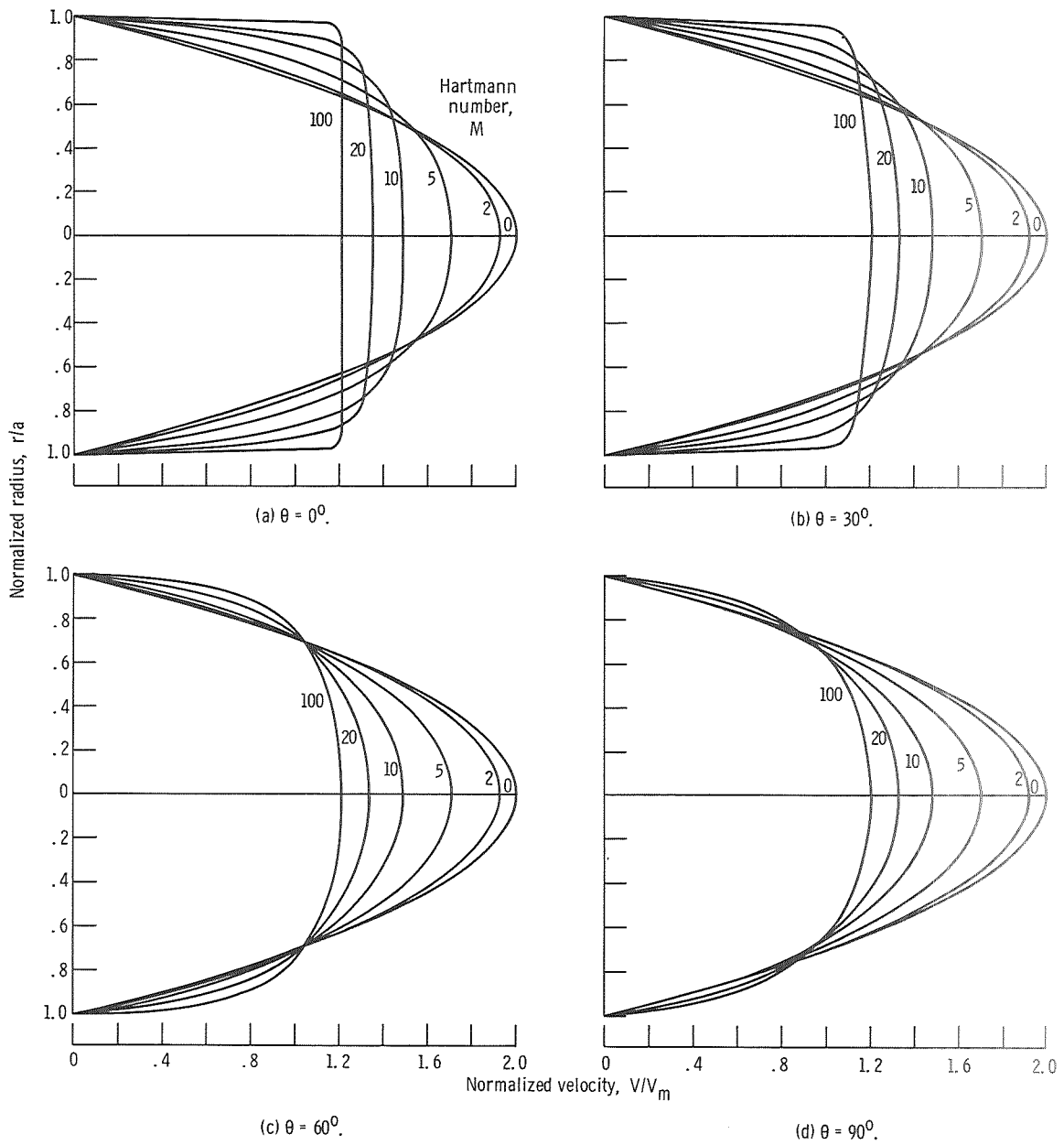


Figure 7. - Normalized velocity profiles for conducting wall with wall-to-fluid electrical conductivity ratio σ_w/σ_f of 0.1 and flowmeter pipe outer-to-inner radius ratio b/a of 1.35.

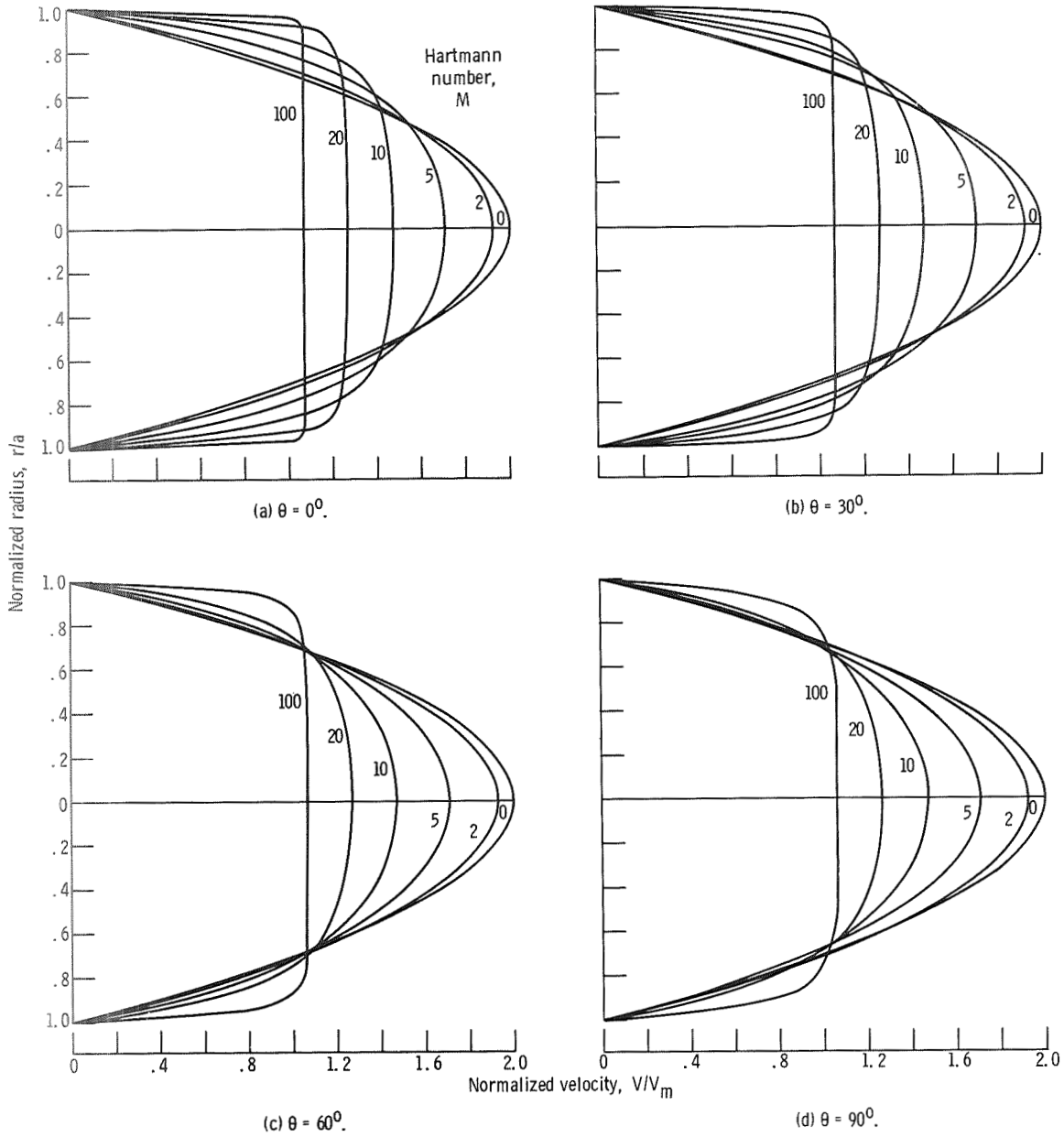


Figure 8. - Normalized velocity profiles for conducting wall with wall-to-fluid electrical conductivity ratio σ_w/σ_f of 2.0 and flowmeter pipe outer-to-inner radius ratio b/a of 1.05.

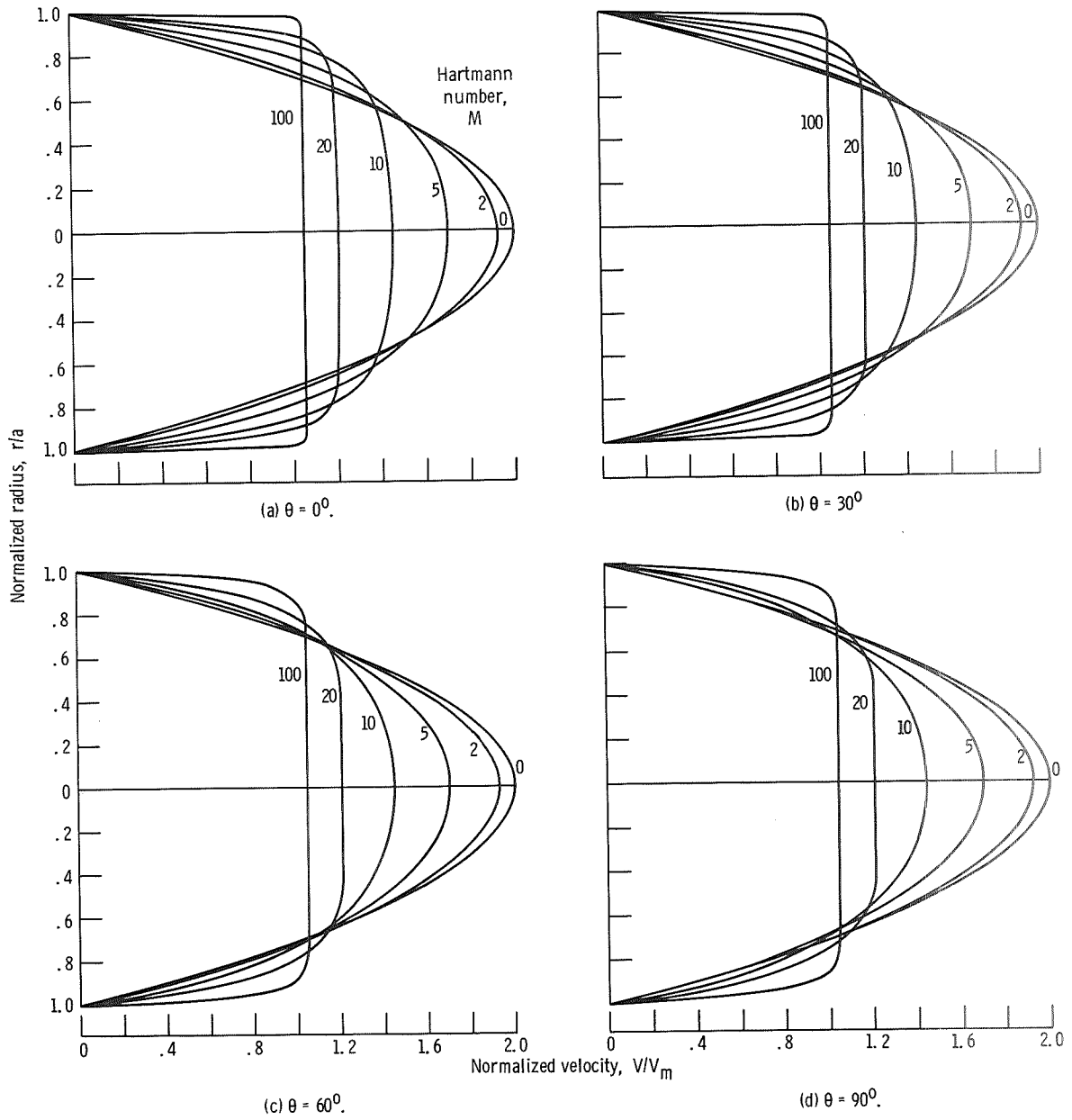


Figure 9. - Normalized velocity profiles for conducting wall with wall-to-fluid electrical conductivity ratio σ_w/σ_f of 2.0 and flowmeter pipe outer-to-inner radius ratio b/a of 1.35.

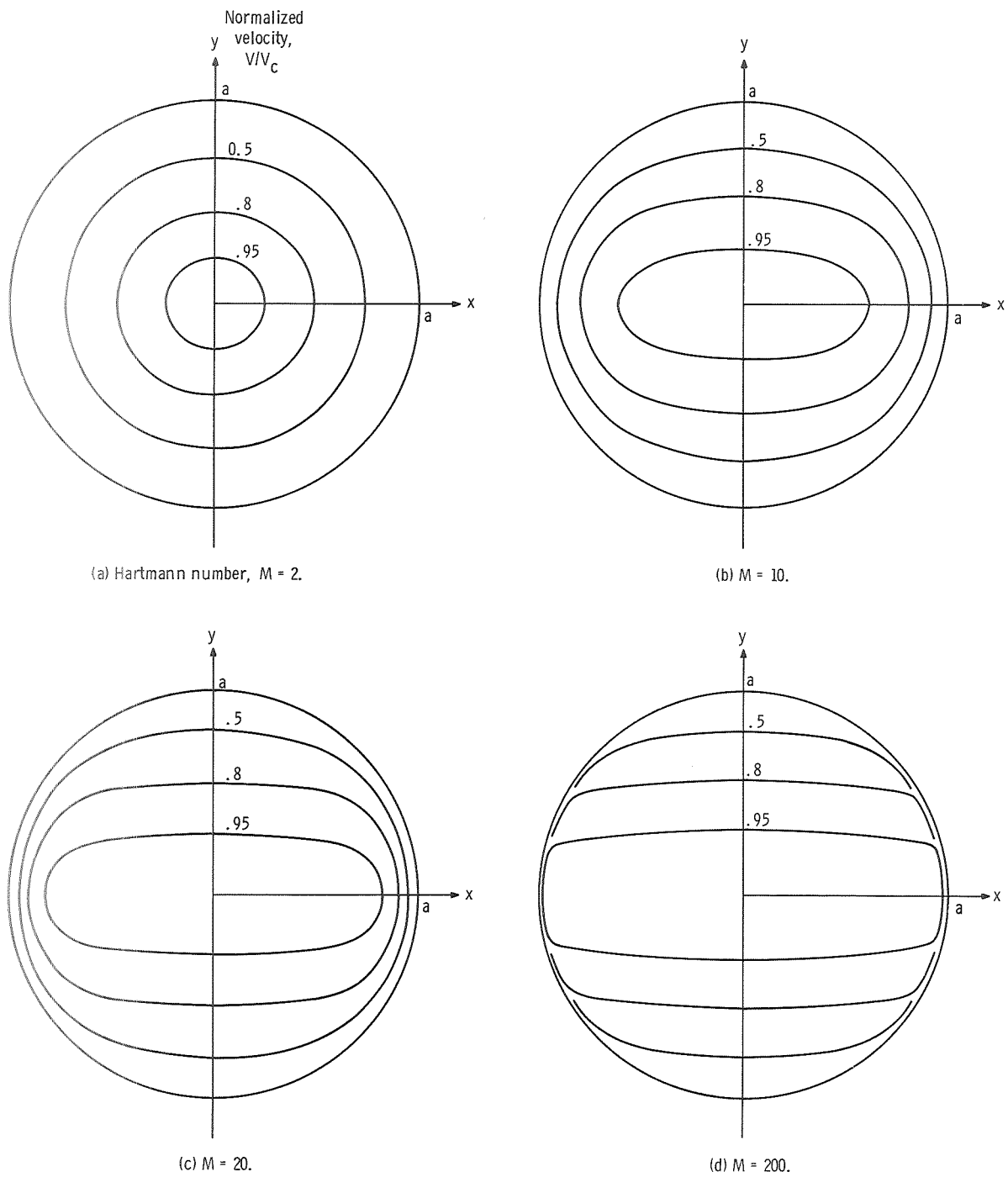
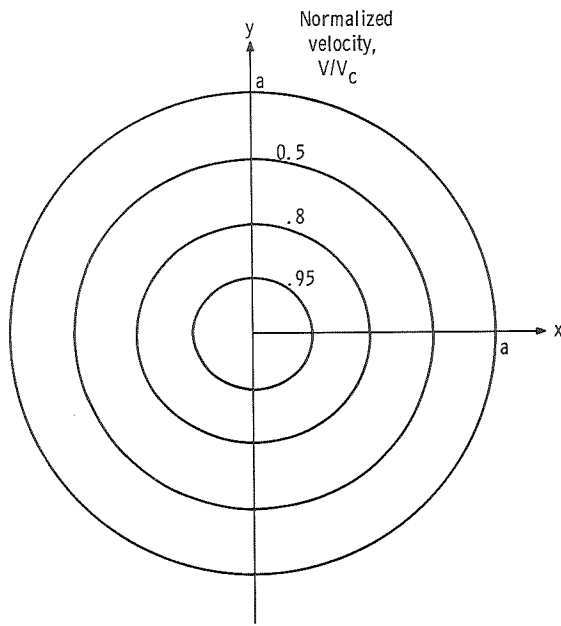
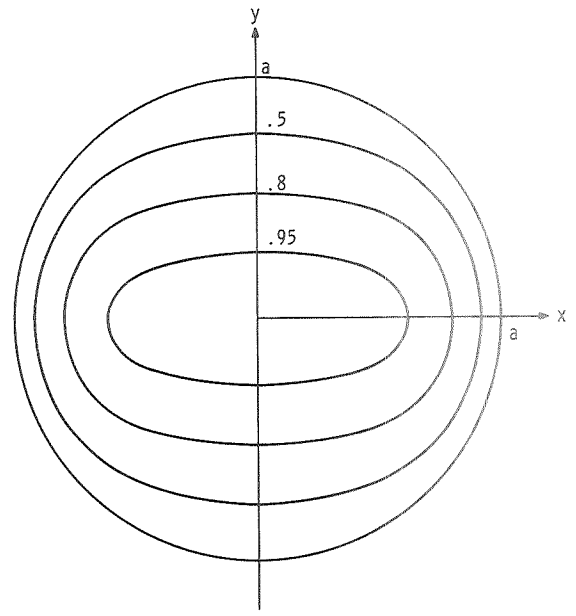


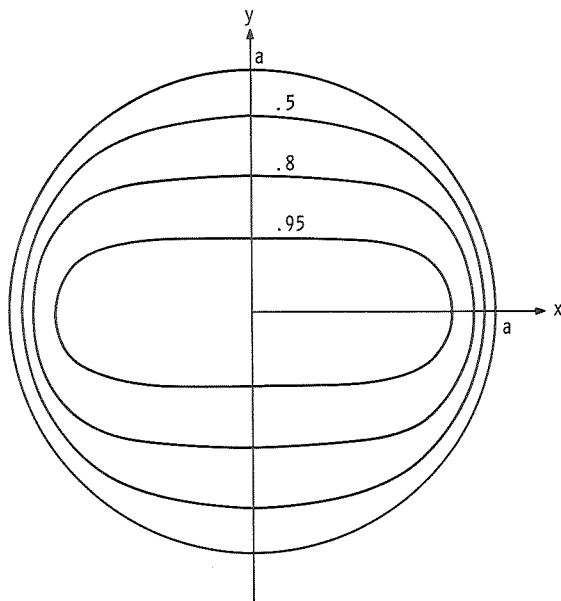
Figure 10. - Normalized velocity contours for nonconducting wall.



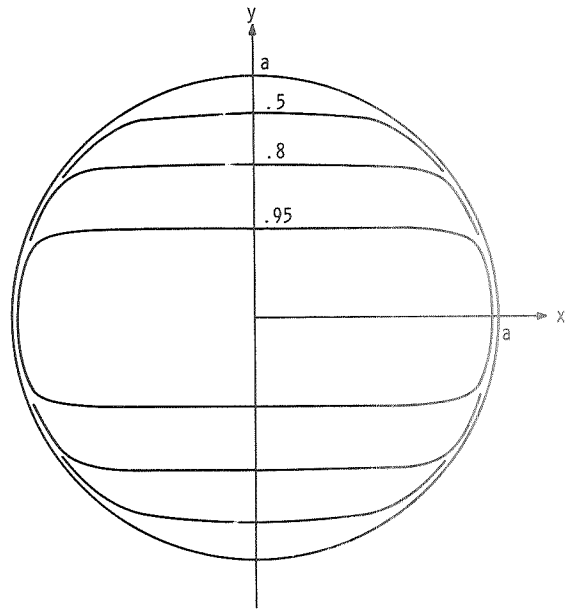
(a) Hartmann number, $M = 2$.



(b) $M = 10$.



(c) $M = 20$.



(d) $M = 200$.

Figure 11. - Normalized velocity contours for conducting wall with wall-to-fluid electrical conductivity ratio σ_w/σ_f of 0.1 and flowmeter pipe outer-to-inner radius ratio b/a of 1.05.

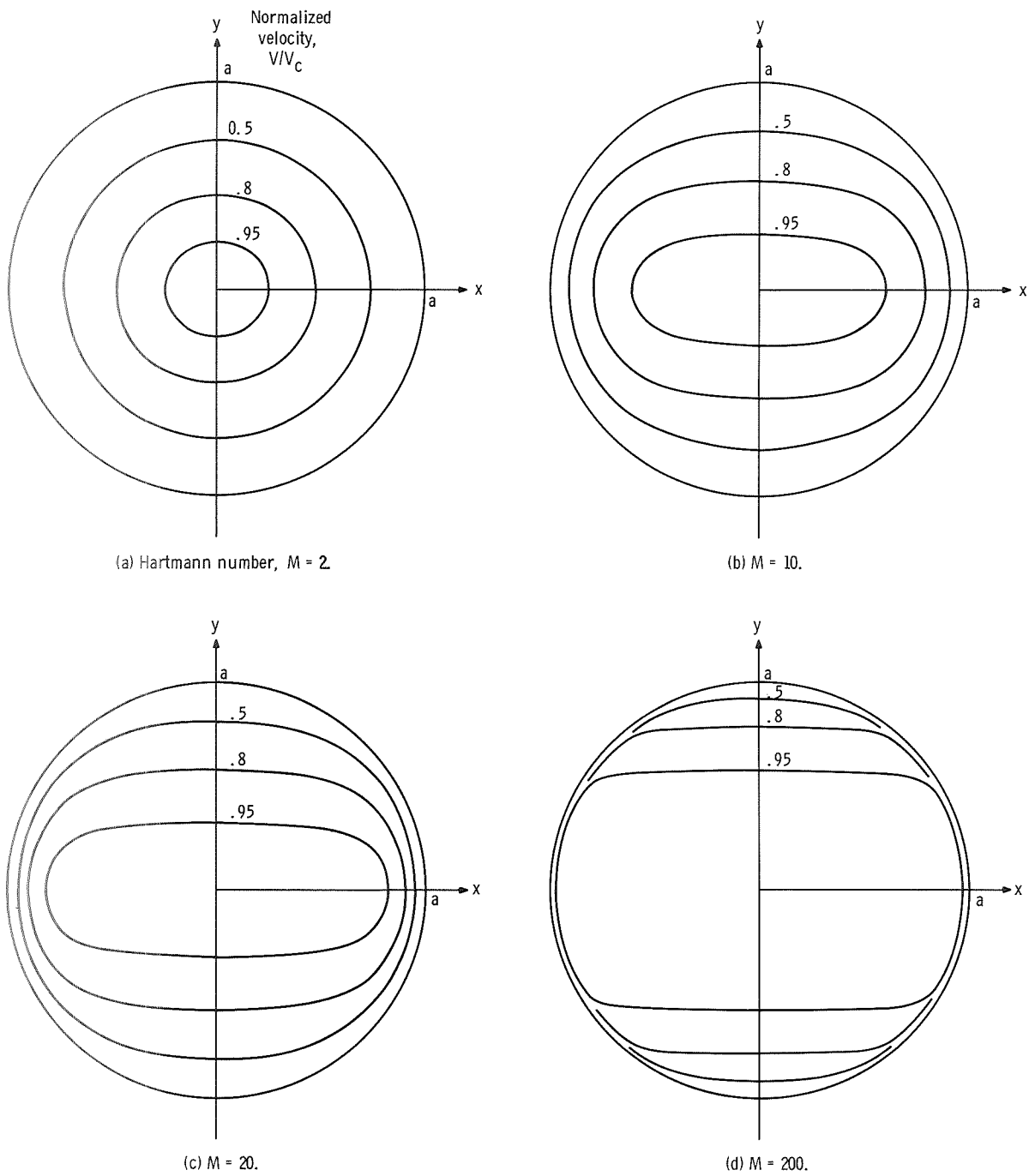


Figure 12. - Normalized velocity contours for conducting wall with wall-to-fluid electrical conductivity ratio σ_w/σ_f of 0.1 and flowmeter pipe outer-to-inner radius ratio b/a of 1.35.

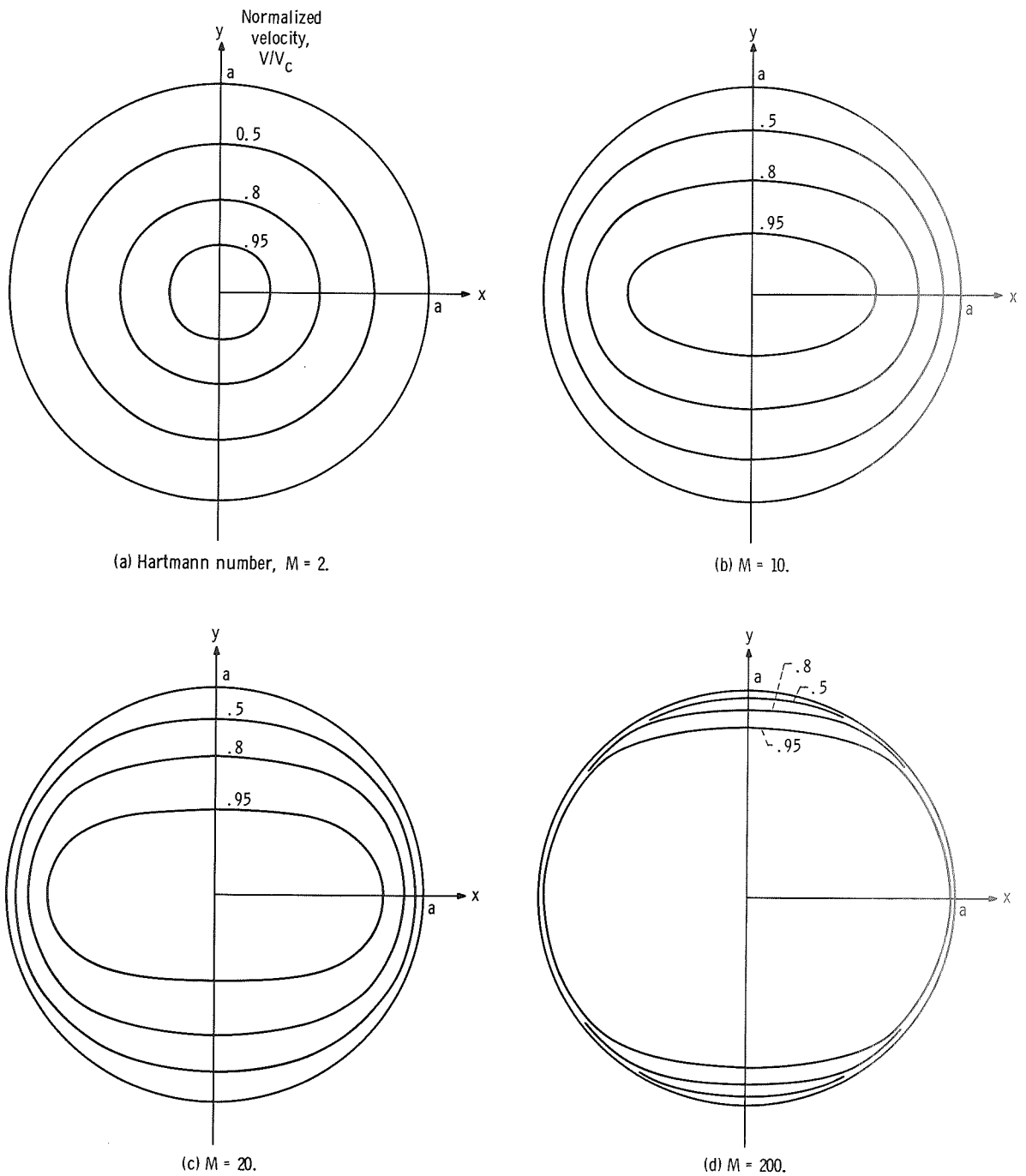
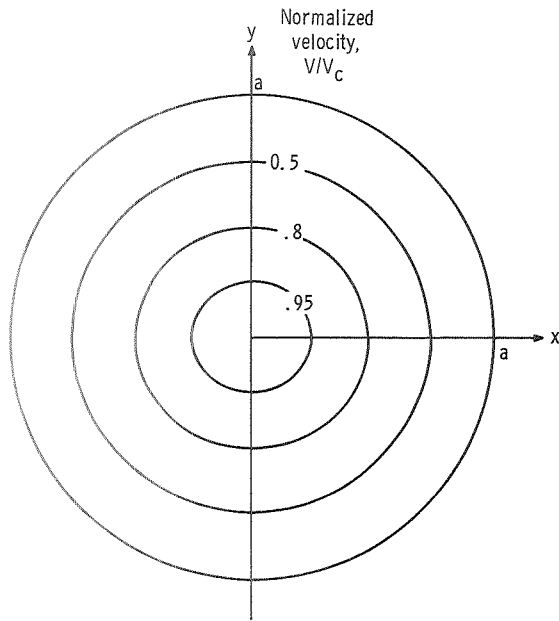
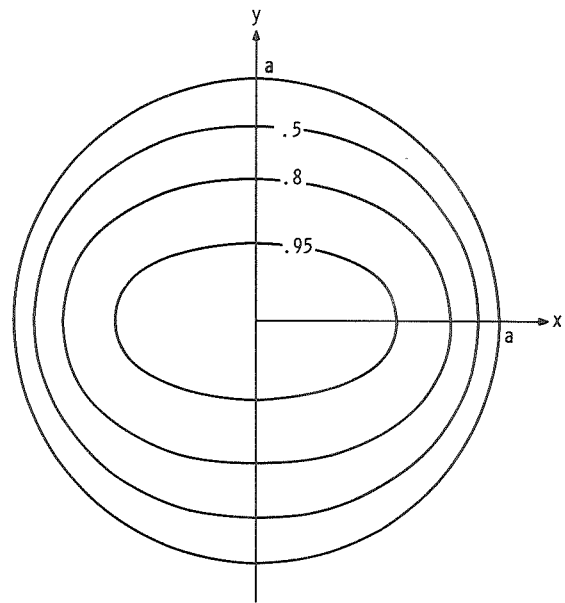


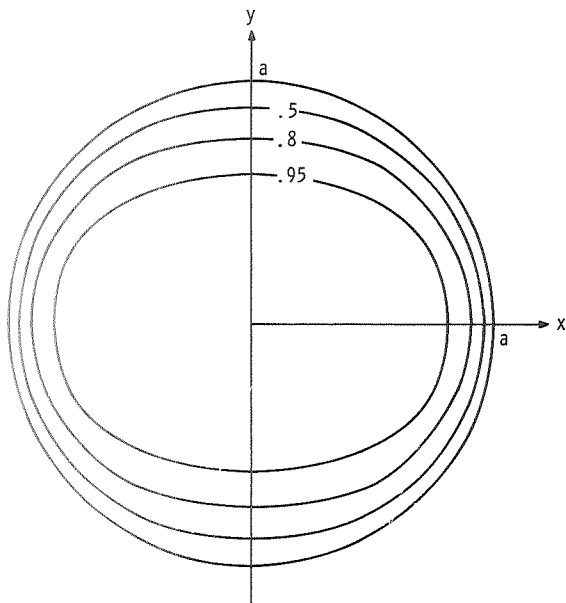
Figure 13. - Normalized velocity contours for conducting wall with wall-to-fluid electrical conductivity ratio σ_w/σ_f of 2.0 and flowmeter pipe outer-to-inner radius ratio b/a of 1.05.



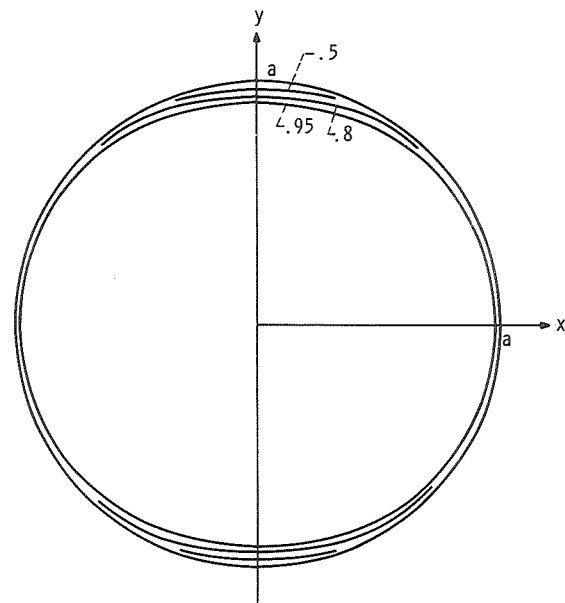
(a) Hartmann number, $M = 2$.



(b) $M = 10$.



(c) $M = 20$.



(d) $M = 200$.

Figure 14. - Normalized velocity contours for conducting wall with wall-to-fluid electrical conductivity ratio σ_w/σ_f of 2.0 and flowmeter pipe outer-to-inner radius ratio b/a of 1.35.

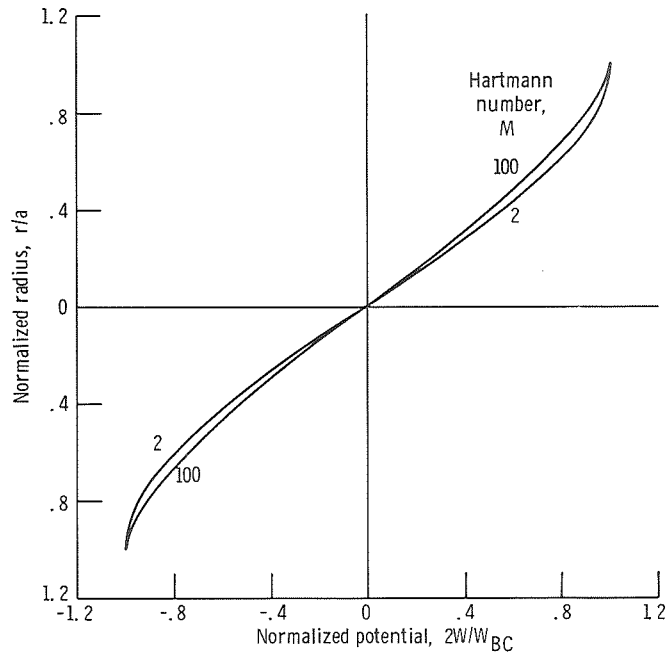


Figure 15. - Normalized potential distribution along y-axis of flowmeter for nonconducting wall.

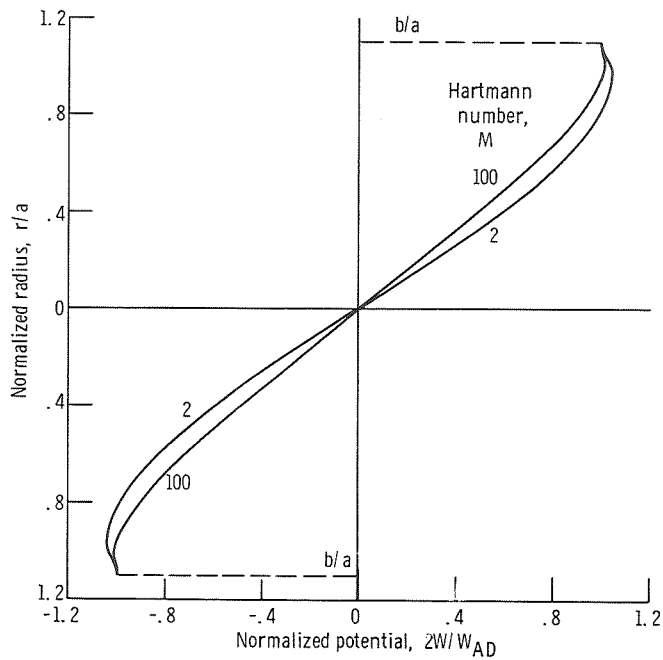


Figure 16. - Normalized potential distribution along y-axis of flowmeter for conducting wall with wall-to-fluid electrical conductivity ratio σ_w/σ_f of 0.1 and flowmeter pipe outer-to-inner radius ratio b/a of 1.05.

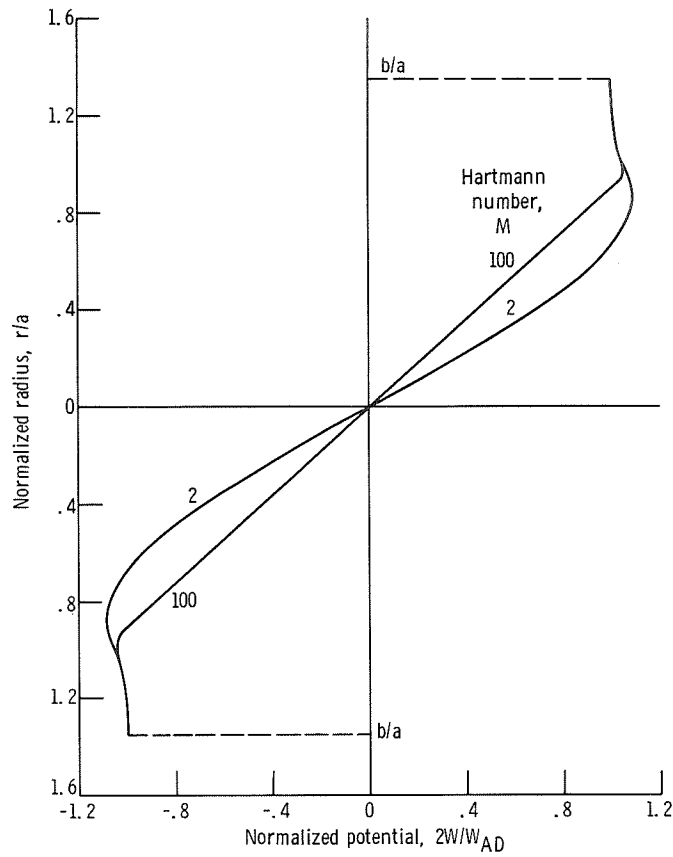


Figure 17. - Normalized potential distribution along y-axis of flowmeter for conducting wall with wall-to-fluid electrical conductivity ratio σ_w/σ_f of 2.0 and flowmeter pipe outer-to-inner radius ratio b/a of 1.35.

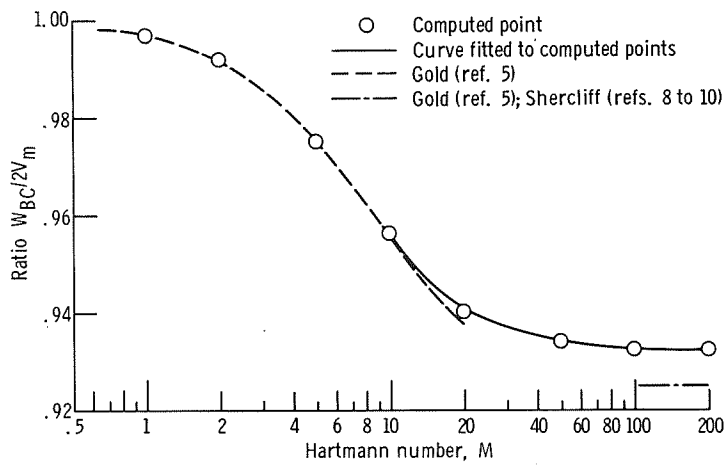


Figure 18. - Calibration curve for electromagnetic flowmeter - nonconducting wall.

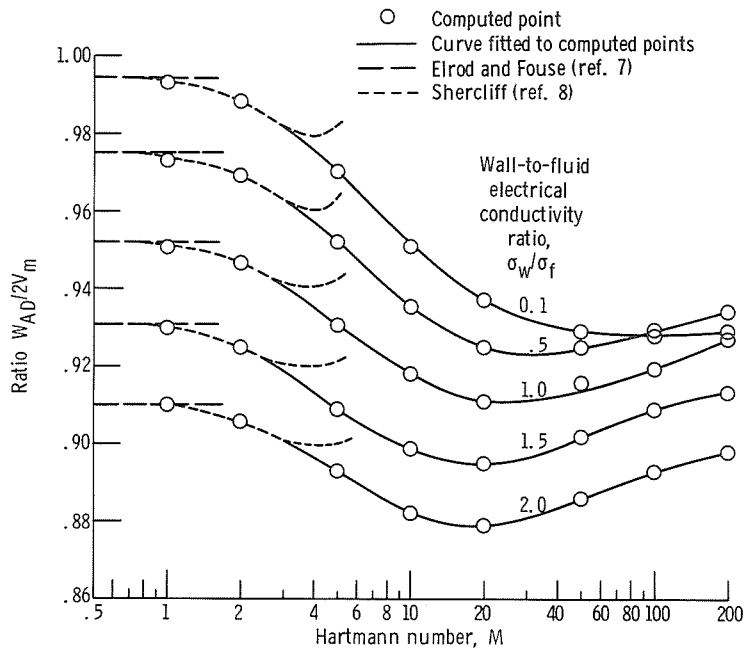


Figure 19. - Calibration curve for electromagnetic flowmeter - conducting wall with flowmeter pipe outer-to-inner radius ratio b/a of 1.05.

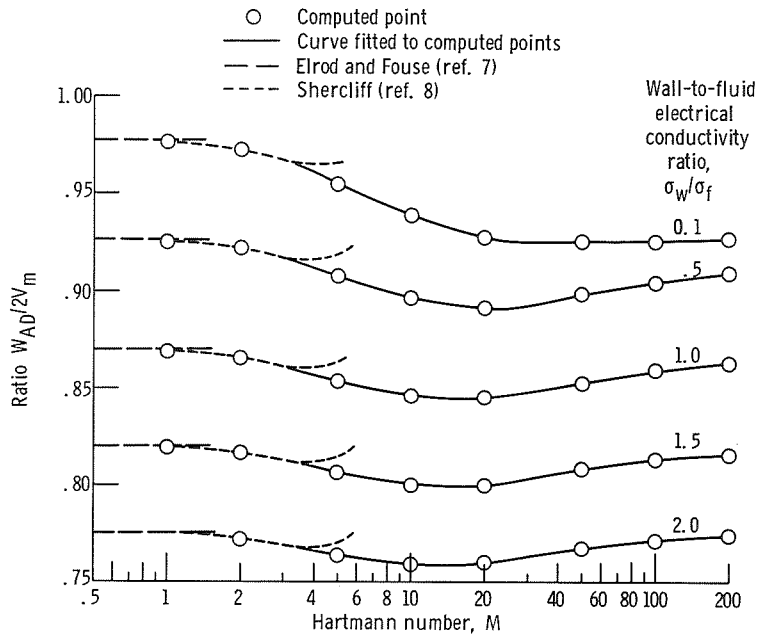


Figure 20. - Calibration curve for electromagnetic flowmeter - conducting wall with flowmeter pipe outer-to-inner radius ratio b/a of 1.15.

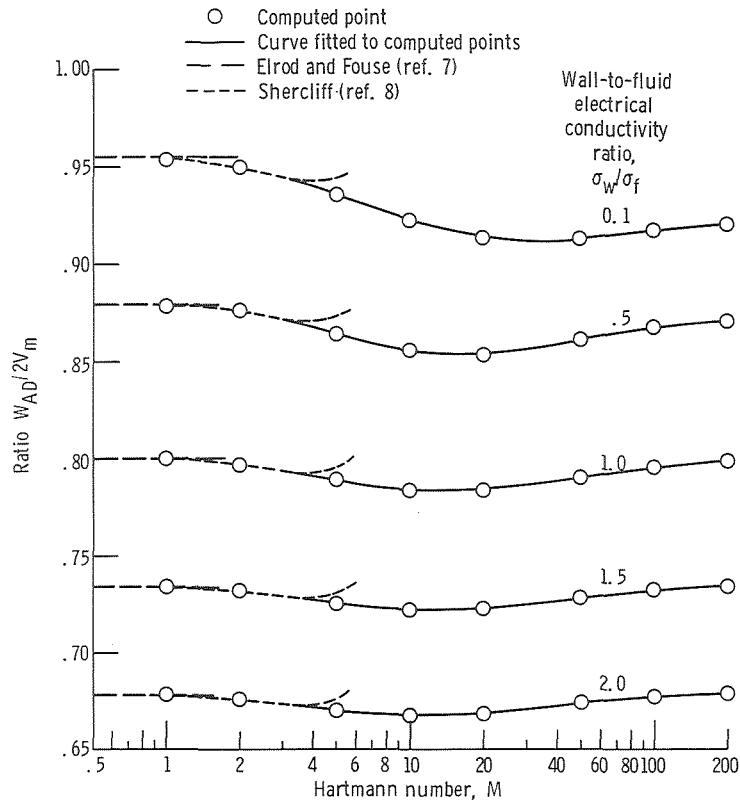


Figure 21. - Calibration curve for electromagnetic flowmeter - conducting wall with flowmeter pipe outer-to-inner radius ratio b/a of 1.25.

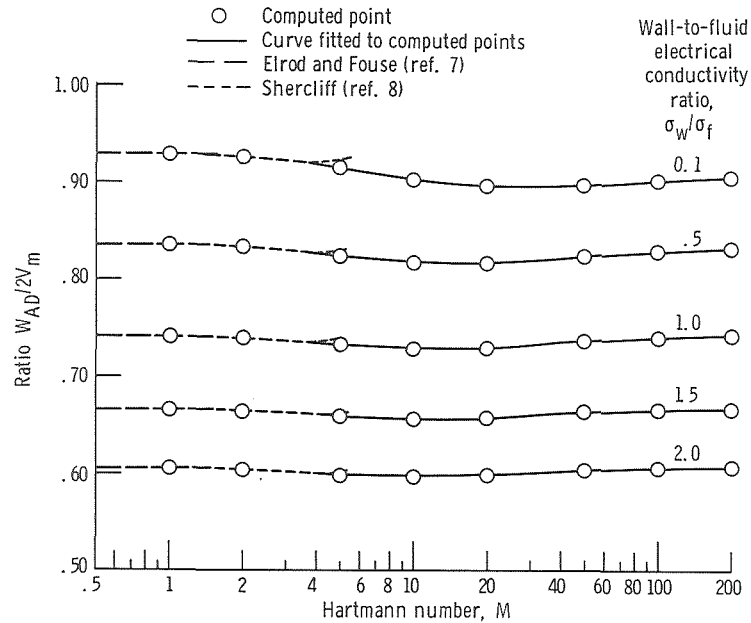


Figure 22. - Calibration curve for electromagnetic flowmeter - flowmeter pipe outer-to-inner radius ratio b/a of 1.35.

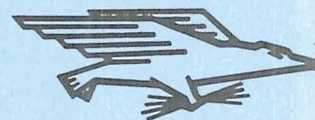
NATIONAL AERONAUTICS AND SPACE ADMINISTRATION

WASHINGTON, D. C. 20546

OFFICIAL BUSINESS

PENALTY FOR PRIVATE USE \$300

FIRST CLASS MAIL



POSTAGE AND FEES PAID
NATIONAL AERONAUTICS AND
SPACE ADMINISTRATION

POSTMASTER: If Undeliverable (Section 158
Postal Manual) Do Not Return

"The aeronautical and space activities of the United States shall be conducted so as to contribute . . . to the expansion of human knowledge of phenomena in the atmosphere and space. The Administration shall provide for the widest practicable and appropriate dissemination of information concerning its activities and the results thereof."

— NATIONAL AERONAUTICS AND SPACE ACT OF 1958

NASA SCIENTIFIC AND TECHNICAL PUBLICATIONS

TECHNICAL REPORTS: Scientific and technical information considered important, complete, and a lasting contribution to existing knowledge.

TECHNICAL NOTES: Information less broad in scope but nevertheless of importance as a contribution to existing knowledge.

TECHNICAL MEMORANDUMS: Information receiving limited distribution because of preliminary data, security classification, or other reasons.

CONTRACTOR REPORTS: Scientific and technical information generated under a NASA contract or grant and considered an important contribution to existing knowledge.

TECHNICAL TRANSLATIONS: Information published in a foreign language considered to merit NASA distribution in English.

SPECIAL PUBLICATIONS: Information derived from or of value to NASA activities. Publications include conference proceedings, monographs, data compilations, handbooks, sourcebooks, and special bibliographies.

TECHNOLOGY UTILIZATION PUBLICATIONS: Information on technology used by NASA that may be of particular interest in commercial and other non-aerospace applications. Publications include Tech Briefs, Technology Utilization Reports and Technology Surveys.

Details on the availability of these publications may be obtained from:

SCIENTIFIC AND TECHNICAL INFORMATION OFFICE

NATIONAL AERONAUTICS AND SPACE ADMINISTRATION

Washington, D.C. 20546